



KMT2C deficiency promotes small cell lung cancer metastasis through DNMT3A-mediated epigenetic reprogramming

Feifei Na^{1,10}, Xiangyu Pan^{2,10}, Jingyao Chen^{2,10}, Xuelan Chen^{2,10}, Manli Wang², Pengliang Chi², Liting You³, Lanxin Zhang², Ailing Zhong², Lei Zhao², Siqi Dai², Mengsha Zhang², Yiyun Wang², Bo Wang², Jianan Zheng², Yuying Wang², Jing Xu², Jian Wang², Baohong Wu², Mei Chen², Hongyu Liu², Jianxin Xue¹, Meijuan Huang¹, Youling Gong¹, Jiang Zhu¹, Lin Zhou¹, Yan Zhang¹, Min Yu¹, Panwen Tian⁴, Mingyu Fan⁵, Zhenghao Lu^{1,6}, Zhihong Xue¹, Yinglan Zhao¹, Hanshuo Yang², Chengjian Zhao², Yuan Wang^{1,2}, Junhong Han^{1,2}, Shengyong Yang², Dan Xie^{1,2}, Lu Chen^{1,2}, Qian Zhong^{1,2}, Musheng Zeng⁷, Scott W. Lowe^{1,8,9}, You Lu^{1,2}, Yu Liu^{1,2}, Yuquan Wei² and Chong Chen^{1,2}✉

Small cell lung cancer (SCLC) is notorious for its early and frequent metastases, which contribute to it as a recalcitrant malignancy. To understand the molecular mechanisms underlying SCLC metastasis, we generated SCLC mouse models with orthotopically transplanted genome-edited lung organoids and performed multiomics analyses. We found that a deficiency of KMT2C, a histone H3 lysine 4 methyltransferase frequently mutated in extensive-stage SCLC, promoted multiple-organ metastases in mice. Metastatic and KMT2C-deficient SCLC displayed both histone and DNA hypomethylation. Mechanistically, KMT2C directly regulated the expression of DNMT3A, a de novo DNA methyltransferase, through histone methylation. Forced DNMT3A expression restrained metastasis of KMT2C-deficient SCLC through repressing metastasis-promoting MEIS/HOX genes. Further, S-(5'-adenosyl)-L-methionine, the common cofactor of histone and DNA methyltransferases, inhibited SCLC metastasis. Thus, our study revealed a concerted epigenetic reprogramming of KMT2C- and DNMT3A-mediated histone and DNA hypomethylation underlying SCLC metastasis, which suggested a potential epigenetic therapeutic vulnerability.

Metastasis is a hallmark of cancer and the leading cause of cancer-related death. It has been proposed that only a small portion of primary tumor cells can complete a series of steps for metastasis¹. Once tumor cells become metastatic, they can keep this capacity stable, which suggests that cell-intrinsic alterations, including genetic and epigenetic dysregulation, might underlie the transition. However, there is mounting evidence showing that there are few metastasis-specific mutations compared to corresponding primary tumors^{2–4}. Paradoxically, metastatic tumor cells display distinct gene signatures^{5,6}. The most parsimonious explanation might be that tumor cells gain epigenetic ‘drivers’ during metastatic progress, which reprogram the genome for the expression regulation of metastasis-associated genes^{4,7}. However, these putative epigenetic metastasis drivers remain elusive.

Small cell lung cancer (SCLC), a lethal lung malignancy with distinct neuroendocrine (NE)-like features, is exceptional^{8,9}. Arguably, SCLC is the most metastatic human cancer, and more than 70% of

individuals with SCLC have metastases at diagnosis⁸. The early and massive metastasis together with invariable chemotherapy treatment relapse makes SCLC a recalcitrant malignancy with a median survival of just 7 months¹⁰. It has been reported that neuronal lineage marker genes ASCL1 and NEUROD1 are required for metastasis of some SCLCs^{11,12}. A breakthrough in the study of SCLC metastasis was discovering that amplification and/or overexpression of NFIB, a transcription factor, promoted SCLC metastasis in mice^{13,14}. NFIB creates global chromatin accessibility and promotes the expression of metastasis-promoting neuronal genes. However, following studies showed that NFIB is only upregulated in some SCLC metastases, and there must be NFIB-independent mechanisms for other SCLC metastases, which needs further study¹⁵.

The early and massive metastases make surgery unfavorable for individuals with SCLC, which leads to limited clinical samples for research and enhances the importance of animal models recapitulating these pathological features^{16,17}. Here, we report

¹Department of Thoracic Oncology, State Key Laboratory of Biotherapy and Cancer Center, West China Hospital, Sichuan University, Chengdu, China.

²State Key Laboratory of Biotherapy and Cancer Center, West China Hospital, Sichuan University, Chengdu, China. ³Department of Laboratory Medicine, West China Hospital, Sichuan University, Chengdu, China. ⁴Department of Respiratory and Critical Care Medicine, West China Hospital of Sichuan University, Chengdu, China. ⁵Lung Cancer Treatment Center, State Key Laboratory of Biotherapy and Cancer Center, West China Hospital, Sichuan University, Chengdu, China. ⁶Chengdu OrganoidMed Medical Laboratory, West China Health Valley, Chengdu, China. ⁷State Key Laboratory of Oncology in South China, Collaborative Innovation Center for Cancer Medicine, Guangdong Key Laboratory of Nasopharyngeal Carcinoma Diagnosis and Therapy, Sun Yat-Sen University Cancer Center, Guangzhou, China. ⁸Cancer Biology and Genetics Program, Memorial Sloan Kettering Cancer Center, New York, NY, USA. ⁹Howard Hughes Medical Institute, Chevy Chase, MD, USA. ¹⁰These authors contributed equally: Feifei Na, Xiangyu Pan, Jingyao Chen, Xuelan Chen.

✉e-mail: chongchen@scu.edu.cn

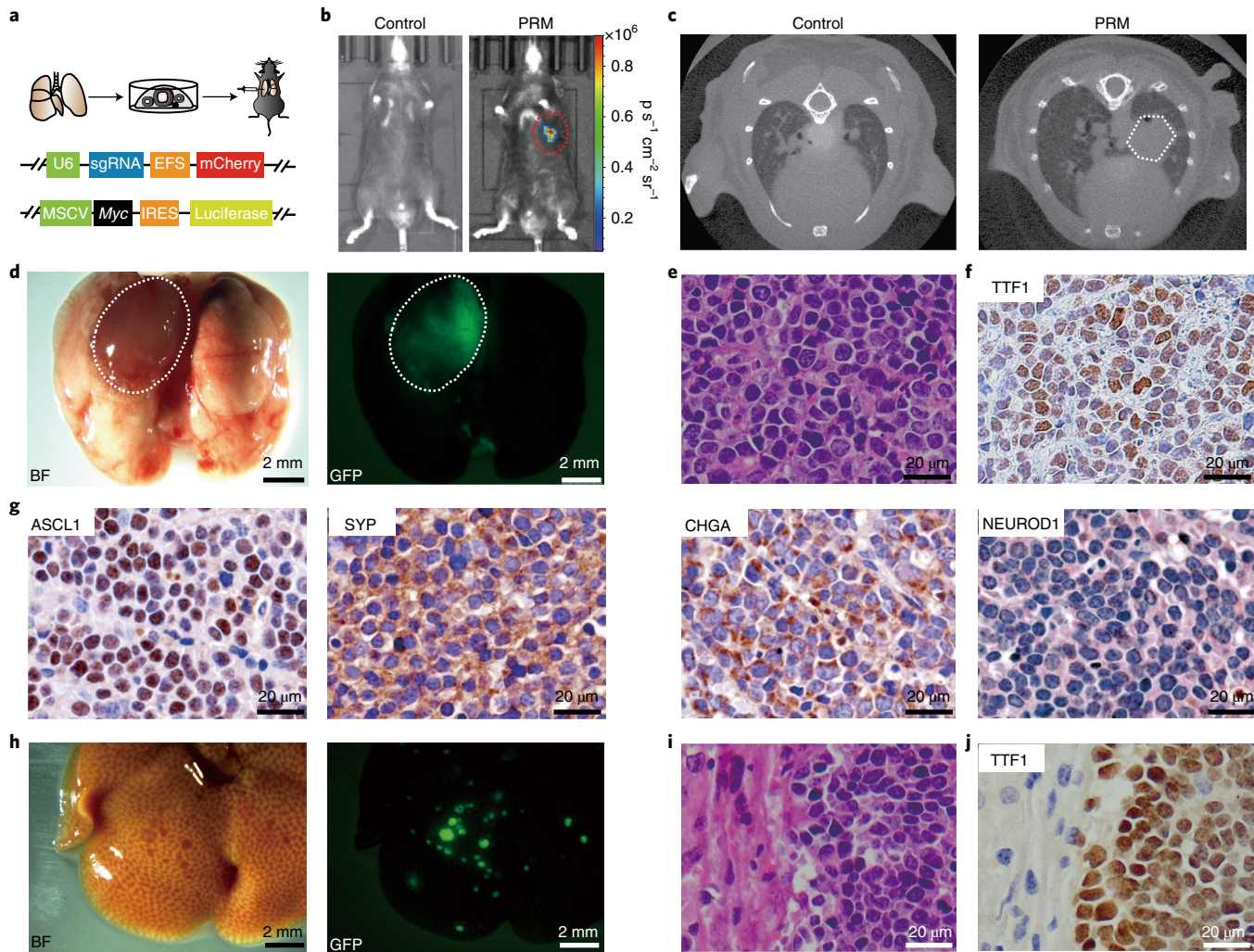


Fig. 1 | Generating primary and orthotopic SCLC with metastases with genome-edited lung organoids in mice. **a**, Top, schematic of the organoid-based strategy for generating primary and orthotopic SCLC in immunocompetent mice. Bottom, schematic of the constructs for expressing sgRNAs and Myc; MSCV, murine stem cell virus; IRES, internal ribosome entry site. **b**, Representative bioluminescent images of mice transplanted with PRM organoids at 3 months after transplantation. **c**, Representative micro-CT images of PRM-recipient mice. **d**, Left, representative brightfield (BF) image of the lungs of a PRM recipient. The lesion on the left lung is indicated, and a representative fluorescent image of the lungs of the PRM recipient is shown on the right; ($n=4$ mice). **e**, Representative hematoxylin and eosin (H&E) staining of a lung section from a PRM mouse ($n=4$ mice). **f**, Representative staining of TTF1 in a lung section from a PRM mouse ($n=4$ mice). **g**, Representative IHC staining of ASCL1, SYP, CHGA and NEUROD1 in lung sections of PRM mice ($n=4$ mice). **h**, Representative brightfield (left) and fluorescent (right) images showing metastatic lesions in the liver of a PRM mouse ($n=4$ mice). **i**, Representative H&E staining of the liver ($n=4$ mice). **j**, Representative TTF1 staining of the liver ($n=4$ mice).

organoid-mediated, primary, orthotopic and driver-defined SCLC mouse models, which faithfully represent the early and massive metastases observed in individuals with SCLC. Through multiomics assays and functional studies of this model, we uncovered a KMT2C-loss-initiated epigenetic reprogramming involving both histone and DNA hypomethylation underlying SCLC metastasis, which suggests a potentially targetable susceptibility of this malignancy.

Results

Primary SCLC models with genome-edited lung organoids. To mimic the pathology of human SCLC, especially its massive distal metastases, we created a strategy to generate primary, orthotopic and driver-defined SCLC in mice with genome-edited lung organoids (Fig. 1a). Briefly, organoids were cultured from lung tissues of adult C57B/L6 mice, with Cas9 and single guide RNAs (sgRNAs) introduced to disrupt genes associated with human

SCLC (Extended Data Fig. 1a,b). Once orthotopically transplanted into the lungs of congenic recipients, the *sgTrp53; sgRb1; Myc; Cas9* (PRM) lung organoids formed a lesion in the lung, which was monitored by luciferase live imaging and micro-computed tomography (micro-CT; Fig. 1b,c). Biopsy showed a single lesion with specific green fluorescent protein (GFP) expression, which indicated that the tumor was derived from the transplanted organoids, at the injection site (Fig. 1d). These single primary tumors, which are in contrast to the numerous lesions in the traditional genetically engineered mouse lung cancer models, precisely recapitulate human disease, which generally develops from a single or limited number of primary lesions. The lesions were mostly composed of tumor cells with small size, scant cytoplasm, granular nuclear chromatin and frequent mitosis, suggesting that these tumors were SCLC (Fig. 1e). These tumor cells were positive for TTF1 and multiple SCLC diagnostic markers, such as ASCL1, SYP, and CHGA, and KI67 (Fig. 1f,g and Extended Data Fig. 1c). However, they were

NEUROD1 negative, suggesting that PRM tumors were the classic ASCL1⁺ NE SCLC¹⁸.

Massive distal metastasis is a key feature of human SCLC, which significantly affects clinical treatments of this disease⁸. In all mice with PRM tumors, numerous metastatic lesions were observed in the liver and lymph nodes, the most common sites of SCLC metastasis in humans (Fig. 1h and Extended Data Fig. 1d). Histological analysis revealed SCLC features of metastatic lesions (Fig. 1i,j and Extended Data Fig. 1e,f). Immunohistochemical (IHC) staining showed that metastatic tumors in both liver and lymph nodes were positive for diagnostic markers, indicating that these metastases maintained the pathology of primary tumors as classic NE type of SCLC (Extended Data Fig. 1g,h).

Single-cell RNA sequencing (scRNA-seq) reveals metastasis trajectory. Given previous reports suggesting a role of global chromatin accessibility in SCLC metastasis^{13,14}, we performed assay for transposase accessible chromatin with high-throughput sequencing (ATAC-seq) of SCLC cells from the primary lesion and liver metastases in the same mice. The results showed that chromatin openness is reduced in metastatic tumor cells, which suggests that there may a distinct mechanism underlying SCLC metastasis (Extended Data Fig. 2a–c and Supplementary Table 1).

To explore the molecular reprogramming underlying metastasis, scRNA-seq was used to assess the primary tumor and metastasis sites (liver) of the same mouse. The cell populations were recognized by expression of conventional marker genes (Fig. 2a, Extended Data Fig. 2d and Supplementary Table 2). While some tumor cells from the lung overlapped with those from the liver, some were specific to the primary tumor, which suggested that not all primary tumor cells had the same metastatic capacity (Fig. 2b). While many SCLC markers, such as *Chga*, *Ddc* and *Ncam1*, were ubiquitously expressed, *Ascl1* was highly expressed in all metastatic cells and in a subset of primary-specific populations, and, by contrast, *Neurod1* was mostly expressed in primary-specific SCLC cells (Fig. 2c and Extended Data Fig. 2e). Indeed, *Neurod1*⁺ SCLC cells were completely absent in metastatic cells (Extended Data Fig. 2f), which suggested that *Ascl1*⁺ primary cells might be more metastatic and the cell of origin of multiple metastases.

To reveal the potential cellular and molecular transitions during metastasis, a metastasis trajectory was constructed based on the URD map for *Ascl1*⁺ SCLC cells (Fig. 2d). The trajectory started from the primary tumor-specific cells to metastatic cells. Along the trajectory, the metastatic score, derived from the gene expression signatures of individuals with SCLC with metastases compared to those without metastases, was progressively increased, suggesting that the metastasis trajectory in mice might reflect a metastasis route in humans (Fig. 2e and Supplementary Table 3)¹⁹. A similar pattern was also observed in a metastatic score derived from circulating tumor cell (CTC)-derived xenografts (CDXs) of individuals with SCLC (Extended Data Fig. 2g and Supplementary Table 4)²⁰. Gene signatures of *Ascl1*⁺ SCLC from the metastatic population were associated with inferior outcomes in individuals with SCLC (Extended Data Fig. 2h and Supplementary Table 5). Dynamically expressed genes along the metastasis trajectory were identified and divided into three modules named modules 1–3, which represented the signatures for SCLC at different stages along the trajectory (Fig. 2f, Extended Data Fig. 2i and Supplementary Tables 6 and 7). Significantly more individuals with SCLC with limited disease expressed module 1 genes than those with extensive disease, while, by contrast, significantly more individuals with extensive disease expressed module 3 genes (Fig. 2g and Supplementary Table 8). Individuals with SCLC with high expression of module 1 genes had a better prognosis than those with lower expression (Extended Data Fig. 2j). These data suggest that our metastasis trajectory represents the molecular properties of SCLC metastasis in humans.

KMT2C deficiency is associated with SCLC metastasis. Given the global chromosome remodeling and gene regulation along the metastasis trajectory of SCLC (Extended Data Fig. 2a–c), we reasoned that some epigenetic regulatory genes might play significant roles during the process. Among the primary-specific module 1 genes were nine epigenetic regulatory genes, and all of them were frequently mutated in human SCLC; *KMT2C* (10%) was the top one, followed by *NCOR2*, *DNMT3A* and *KDM5B* (Extended Data Fig. 3a and Supplementary Table 9). Gene set enrichment analysis showed that multiple histone and DNA methylation pathways were significantly negatively enriched in metastatic SCLC cells (Extended Data Fig. 3b and Supplementary Table 10). In The Cancer Genome Atlas (TCGA) cohorts, *KMT2C* mutations were detected in 7% of primary SCLC samples but were detected in 27% of metastatic samples, and, consistently, 17% of the Cancer Cell Line Encyclopedia (CCLE) SCLC cell lines derived from metastases contained mutations in *KMT2C*, while none derived from primary tumors had *KMT2C* mutations (Fig. 3a)^{19,21}. Further, expression levels of *Kmt2c* in metastatic cells were significantly lower than those in primary cells in both mice and humans (Fig. 3b). ATAC-seq showed that the *Kmt2c* locus was closed in metastatic cells, which is associated with reduced expression levels, compared to in primary tumors (Fig. 3c and Supplementary Table 1). Expression levels of *KMT2C* were significantly negatively correlated with the metastatic gene signature in SCLC (Fig. 3d), and low *KMT2C* expression was associated with poor prognosis in individuals with SCLC (Extended Data Fig. 3c).

KMT2C encodes a histone 3 lysine 4 (H3K4) mono- and dimethyltransferase. Western blotting showed that both H3K4me1 and H3K4me2 levels were reduced in metastatic SCLC cells (Extended Data Fig. 3d). Consistently, IHC staining confirmed the downregulation of *KMT2C* expression and the reduced levels of H3K4me1 and H3K4me2 in metastases compared to in primary tumors (Extended Data Fig. 3e). Further, cleavage under targets and tagmentation (CUT&Tag) analyses demonstrated that the global H3K4me1 level of the enhancer regions in the metastatic tumor cells was reduced compared to that observed in primary SCLC cells, which was consistent with the global decrease of chromosome accessibility (Fig. 3e, Extended Data Figs. 2a–c and 3f,g and Supplementary Table 11). Thus, these data suggest that *KMT2C* deficiency and its related epigenetic reprogramming are associated with SCLC metastasis.

KMT2C loss gives rise to a premalignant population ex vivo. To investigate the potential functions of *KMT2C* in SCLC, we transduced sgRNAs targeting *Kmt2c* into lung organoids with Cas9. *Kmt2c* disruption was confirmed by T7 endonuclease (T7E) assay (Extended Data Fig. 3h). *KMT2C* loss significantly promoted the growth of lung organoids (Fig. 3f). In control scramble (sgScr) lung organoids, there were three types of epithelial cells, including *Trp63*⁺ stem cells, *Notch1*⁺ progenitor cells and *Cyp2f2*⁺ differentiated cells (Fig. 3g,h and Supplementary Table 12). A differentiation trajectory could be drawn from the *Trp63*⁺ stem cells to the *Notch1*⁺ progenitor cells and ended at the *Cyp2f2*⁺ differentiated cells. However, in *KMT2C*-deficient lung organoids, the differentiation trajectory was diminished, while the trajectory to the *Mki67*⁺ population was enhanced (Fig. 3g–i). Along the differentiation trajectory, differentiation markers, such as *Notch1* and *Cyp2f2*, were upregulated (Extended Data Fig. 3i). Instead, the expression of SCLC signature genes from humans progressively increased along the *MKI67* trajectory and decreased along the differentiation trajectory (Extended Data Fig. 3i and Supplementary Table 13). The SCLC and metastasis signatures from individuals with SCLC were progressively upregulated along the *MKI67* trajectory and downregulated along the differentiation trajectory (Fig. 3j). These analyses suggest that *KMT2C* loss by itself would lead to a prometastatic status in lung organoids.

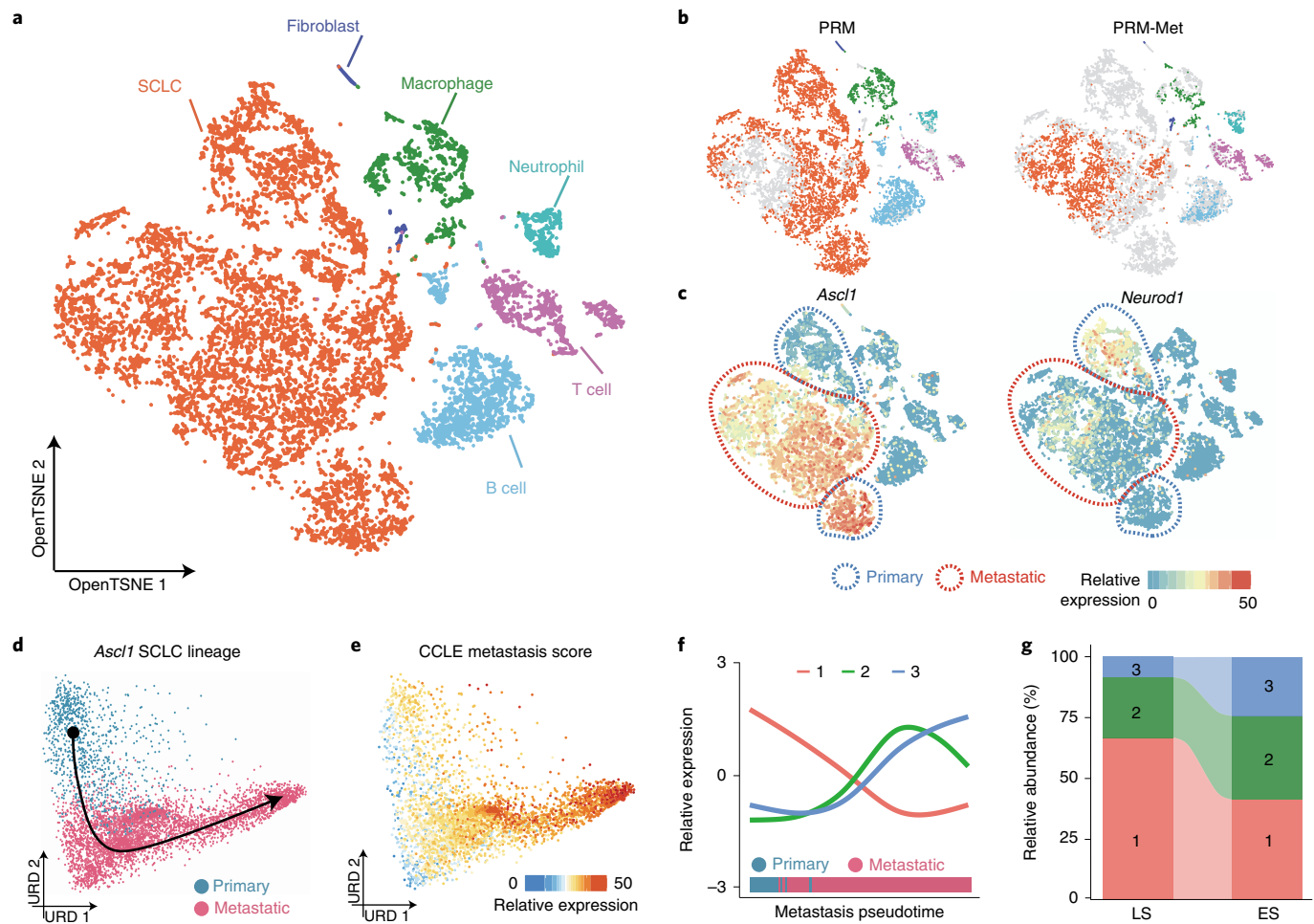


Fig. 2 | A metastasis trajectory of SCLC revealed by single-cell transcriptome analyses. **a**, Open t-distributed stochastic neighbor embedding (OpenTSNE) map of scRNA-seq analyses of SCLC from the lung and liver of the same PRM mouse; 7,925 cells and 3,513 cells were captured from the primary site and metastatic lesion (liver) of the same mouse, respectively. **b**, OpenTSNE plot showing the organ origins from PRM (lung) and PRM metastasis (PRM-Met; liver). **c**, OpenTSNE map showing expression levels of *Ascl1* and *Neurod1* in primary SCLC cells and metastatic SCLC cells. **d**, URD map showing the metastasis trajectory of *Ascl1*⁺ SCLC cells. **e**, URD map showing the CCLE metastasis score projected on the metastasis trajectory. **f**, Dynamically expressed gene modules on the metastasis trajectory. **g**, Alluvial plot showing the composition variation of three molecular subtypes defined by the dynamically expressed gene modules in limited-stage (LS) and extensive-stage (ES) SCLC in the Simpson cohort.

KMT2C restrains SCLC tumorigenesis and metastasis in mice. To test the potential roles of KMT2C in SCLC *in vivo*, *Kmt2c* was repressed by either short hairpin RNA (shRNA) or CRISPR/Cas9, as we reported previously²², together with *Trp53* and *Rb1* sgRNAs and *Myc* overexpression in primary lung organoids (PRMK). PRMK organoids with either sh*Kmt2c* or sg*Kmt2c* displayed significantly increased size and number compared to PRM organoids (Fig. 4a,b). PRM and PRMK premalignant organoids were transplanted into the left lungs of C57BL/6 mice. Luciferase live imaging revealed that there was significantly stronger luciferase signaling in the chests of recipient mice with either sh*Kmt2c* or sg*Kmt2c* organoids than in the chests of control PRM mice (Fig. 4c,d). All sg*Kmt2c* organoid recipient mice died of SCLC with a significantly shorter latency (69 d) than control PRM recipients (126 d). Similarly, all recipients of sh*Kmt2c* organoids developed SCLC and had significantly shorter latency (93 d; Fig. 4e). All KMT2C-deficient tumors resembled the pathology of human SCLC, with strong staining of TTF1 (Extended Data Fig. 4a). PRMK tumors were also positive for ASCL1, CHGA and SYP but negative for NEUROD1, indicating that they are of the classic NE type of SCLC (Extended Data Fig. 4b). These data demonstrate that *Kmt2c* is a bona fide tumor suppressor in SCLC.

Pathological analyses showed that there were massive metastases in multiple organs of the PRMK mice (Fig. 4f,g and Extended Data Fig. 4b). Increased metastases were also observed in other organs, including lymph nodes and kidneys, in the PRMK mice (Fig. 4h,i and Extended Data Fig. 4c,d). CTCs have been suggested to play roles during SCLC metastasis and could be used as diagnostic markers^{20,23}. In both the PRM and PRMK mice, we identified CTCs as CD45⁻mCherry⁺ cells in the peripheral blood, which had specifically high expression of SCLC markers, such as *Ascl1*, *Ncam1*, *Chga* and *Syp* (Extended Data Fig. 4e,f). Frequencies of CTCs were significantly higher in PRMK mice than in PRM mice (Fig. 4j,k). Recently, it has been reported that human SCLC cells could grow axon-like protrusions *in vitro*, which had been proposed to promote metastasis²⁴. Consistent with the previous observation in two-dimensional cultured cell lines, we observed significantly more such axon-like protrusions in the three-dimensional cultured PRMK SCLC organoids than in the PRM organoids (Fig. 4l,m). Taken together, these data strongly suggest that KMT2C deficiency promotes SCLC metastasis in mice.

Epigenetic reprogramming associated with metastasis. As an H3K4 mono- and dimethyltransferase, KMT2C loss reduced the

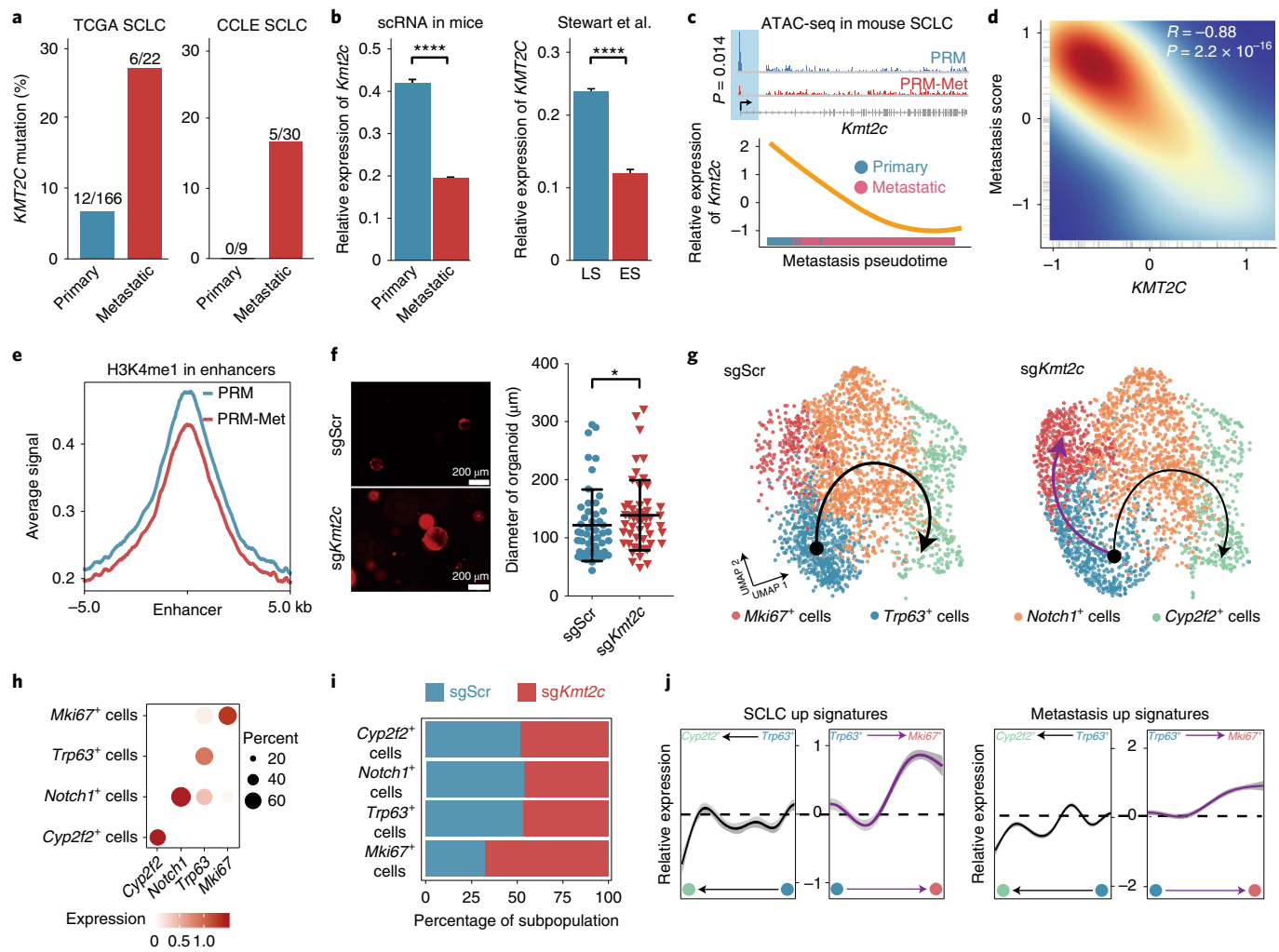


Fig. 3 | KMT2C deficiency is associated with SCLC metastasis and gives rise to a premalignant population in lung organoids. **a**, Bar graph showing the mutation frequencies of *KMT2C* in primary and metastatic SCLC from TCGA (left) and CCLE cohorts (right). **b**, Bar graph showing the relative expression levels of *Kmt2c* in mouse primary and metastatic (left) and human LS and ES (right) SCLC cells²⁰. Data are shown as mean ± s.e.; $n = 2,365$, primary; $n = 13,798$, metastatic; $n = 10,000$, LS SCLC; $n = 2,000$, ES SCLC. Significance was assessed by Wilcoxon signed-rank test. **c**, Top, Integrative Genomics Viewer (IGV) plot showing the distributions of ATAC-seq peaks in the *Kmt2c* locus in PRM and PRM-Met SCLC cells. Bottom, dynamics of relative expression levels of *Kmt2c* on metastasis trajectory. **d**, Scatter plot showing the correlation between the relative expression levels of *KMT2C* and the SCLC metastasis score in individuals with SCLC. $R = -0.88$, $P = 2.2 \times 10^{-16}$. **e**, Levels of H3K4me1 bound at enhancers in PRM and PRM-Met tumor cells, as measured by CUT&Tag analyses; kb, kilobases. **f**, Left, representative fluorescence images of sgScr and sg*Kmt2c* lung organoid growth. Right, diameters of the lung organoids with sgScr or sg*Kmt2c*. Data are shown as mean ± s.d.; $n = 50$, sgScr; $n = 52$, sg*Kmt2c*. Significance was assessed by two-sided Student's *t*-test. **g**, Uniform manifold approximation and projection (UMAP) plots showing populations and trajectories in the lung organoids with sgScr or sg*Kmt2c*. The 2,794 cells and 2,794 cells were captured from the sgScr sample ($n = 1$) and sg*Kmt2c* sample ($n = 1$), respectively. **h**, Dot plot showing the marker genes of each population. **i**, Stacked bar chart showing the percentages of cell populations in sgScr and sg*Kmt2c* organoids. **j**, The dynamic expression levels of SCLC up (left) and metastasis up (right) gene signatures on the development (black line) and malignant differentiation (purple line) trajectories are shown; * $P < 0.05$, *** $P < 0.0001$.

total levels of H3K4me1 and H3K4me2 in SCLC, which was confirmed by both IHC staining and western blotting and was consistent with the disruption of *Kmt2c* in PRMK tumors revealed by RNA-seq (Extended Data Fig. 5a–c). Consistently, CUT&Tag sequencing showed that there was a global H3K4me1 decrease, including in the enhancer and transcription start site (TSS) regions, in the PRMK SCLC cells compared to PRM cells (Fig. 5a, Extended Data Fig. 6a,b and Supplementary Table 14); 93% of the genes with reduced H3K4me1 levels in the PRM metastatic SCLC cells also displayed significantly reduced levels of H3Kme1 in PRMK cells (Fig. 5b). We also observed that H3K4me2 levels across the genome, mostly at the TSS regions, were also downregulated by KMT2C loss

(Fig. 5a, Extended Data Fig. 6c,d and Supplementary Table 15). There were no significant changes in H3K4me3 levels in PRM and PRMK cells (Fig. 5a, Extended Data Fig. 6e,f and Supplementary Table 16). However, global chromatin accessibility was reduced in PRMK tumor cells compared to PRM cells (Fig. 5a, Extended Data Fig. 6g,h and Supplementary Table 17). It was intriguing that overall chromatin accessibility close by KMT2C loss resembled that in metastatic SCLC, and genes with less chromatin accessibility in PRMK tumors were significantly overlapped with those in PRM metastases (Fig. 5c). These data indicate that there was significant epigenetic rewiring by KMT2C loss, which precisely resembled that in metastatic SCLC.

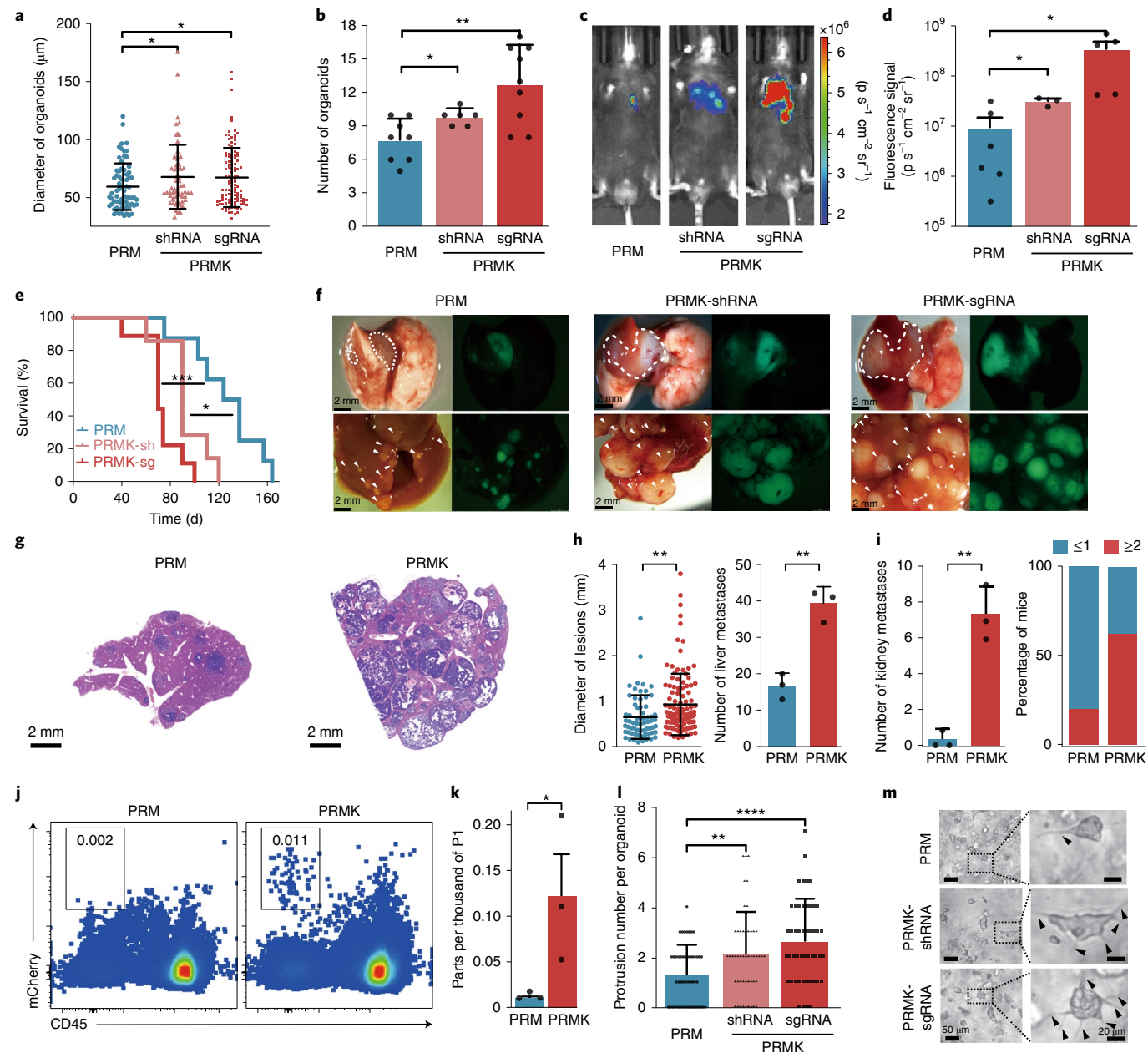


Fig. 4 | KMT2C deficiency promotes tumorigenesis and metastasis of SCLC. **a**, Diameter quantification of premalignant PRM ($n=69$), PRMK-shRNA ($n=64$) and PRMK-sgRNA ($n=115$) lung organoids. Data are shown as mean \pm s.d. Significance was calculated by two-sided Student's *t*-test. **b**, Number of premalignant PRM ($n=8$), PRMK-shRNA ($n=6$) and PRMK-sgRNA ($n=9$) lung organoids. Data are shown as mean \pm s.d. Significance was calculated by two-sided Student's *t*-test. **c**, Representative bioluminescent images of mice transplanted with PRM, PRMK-shRNA or PRMK-sgRNA organoids at 3 months after transplantation. **d**, Luciferase fluorescence signal intensity of PRM ($n=6$), PRMK-shRNA ($n=3$) and PRMK-sgRNA ($n=5$) mice. Data are shown as mean \pm s.e.m. Significance was calculated by two-sided Student's *t*-test. **e**, Kaplan-Meier survival curves of mice transplanted with PRM ($n=8$), PRMK-shRNA ($n=7$) and PRMK-sgRNA ($n=9$) organoids. All curves were analyzed by log-rank test. **f**, Representative brightfield and fluorescence images of the lungs (top) and livers (bottom) of PRM, PRMK-shRNA and PRMK-sgRNA mice. **g**, Representative images of H&E staining of the livers of PRM ($n=4$) and PRMK ($n=4$) mice. **h**, Statistical graphs showing the lesion diameters (left) and number of metastases (right) in the livers of PRM and PRMK mice. Data are shown as mean \pm s.d.; left: $n=66$ PRM and $n=116$ PRMK; right: $n=3$. Significance was calculated by two-sided Student's *t*-test. **i**, Numbers of metastatic lesions in the kidneys of PRM and PRMK mice (left) and percentages of PRM or PRMK mice with indicated numbers of organs with metastases (right). Data are shown as mean \pm s.d.; left, $n=3$. Significance was calculated by two-sided Student's *t*-test. **j**, Representative flow cytometry plots showing the CD45⁺mCherry⁺ CTCs in the peripheral blood of PRM and PRMK mice. **k**, Percentage of CTCs in the peripheral blood of PRM and PRMK mice. P1 represents the CD45⁺ and mCherry⁺ CTC. Data are shown as mean \pm s.e.m.; $n=3$. Significance was calculated by two-sided Student's *t*-test. **l**, Average number of axon-like protrusions per organoid. Data are shown as mean \pm s.d.; $n=49$. Significance was calculated by two-sided Student's *t*-test. **m**, Representative images showing the morphology of the PRM ($n=4$), PRMK-shRNA ($n=4$) and PRMK-sgRNA ($n=4$) SCLC organoids. * $P<0.05$, ** $P<0.01$, *** $P<0.001$, **** $P<0.0001$.

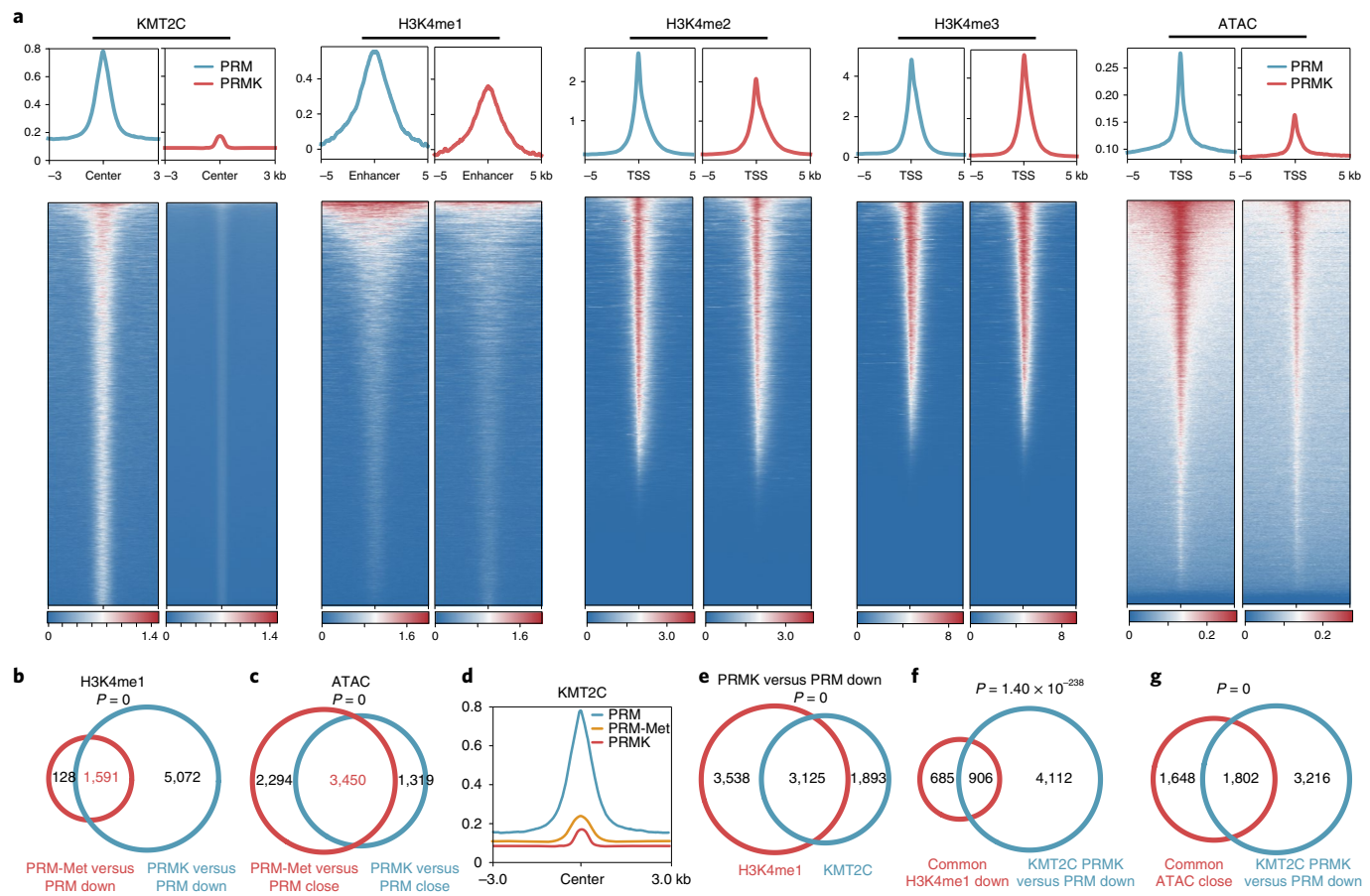


Fig. 5 | Epigenetic reprogramming in *Kmt2c*-mutant SCLC. **a**, Levels of KMT2C bound at the center of peaks, levels of H3K4me1 bound at the enhancer and levels of H3K4me2, H3K4me3 and ATAC bound at the TSS in PRM and PRMK tumor cells, as measured by CUT&Tag analyses. **b**, Venn diagram showing overlapping of the H3K4me1 downregulated genes in PRM metastatic cells compared to in PRM primary cells and the H3K4me1 downregulated genes in PRMK cells compared to in PRM primary cells. The *P* value was calculated by a hypergeometric test. **c**, Venn diagram showing overlapping of the chromatin closed genes in PRM metastatic cells compared to in PRM primary cells and the chromatin close genes in PRMK cells compared to in PRM primary cells. The *P* value was calculated by a hypergeometric test. **d**, Levels of KMT2C bound at the center in PRM, PRM-Met and PRMK tumor cells, as measured by the CUT&Tag analyses. **e**, Venn diagram showing overlapping of H3K4me1 downregulated genes and KMT2C downregulated genes in PRMK cells compared to in PRM SCLC cells. The *P* value was calculated by a hypergeometric test. **f**, Venn diagram showing overlapping of the common genes with reduced H3K4me1 levels in both PRM-Met and PRMK cells and the KMT2C downregulated genes in PRMK compared to PRM SCLC cells. The *P* value was calculated by a hypergeometric test. **g**, Venn diagram showing overlapping of the common genes with closed chromatin accessibility in both PRM-Met and PRMK cells and the KMT2C downregulated genes in PRMK compared to PRM SCLC cells. The *P* value was calculated by a hypergeometric test.

To test how much KMT2C would directly contribute to these epigenetic abnormalities in SCLC metastases, we performed CUT&Tag sequencing of KMT2C in the PRM, PRMK and PRM metastatic SCLC cells. KMT2C is specially bound on the promoter regions and distal intergenic and other regions on the genome (Extended Data Fig. 6i,j and Supplementary Tables 18 and 19). The binding of KMT2C across the genome in PRM metastatic cells was dramatically reduced, which was recapitulated by KMT2C loss (Fig. 5d and Extended Data Fig. 6i). About half of the genes with reduced H3K4me1 levels in PRMK SCLC were directly bound by KMT2C (Fig. 5e). Similarly, those with reduced H3K4me2 were also directly bound by KMT2C (Extended Data Fig. 7a). Further, we found that 56.9% of the common genes with reduced H3K4me1 levels in PRM metastases and PRMK tumors were directly bound by KMT2C (Fig. 5f). Similarly, 52.2% of those with close chromatin accessibility in both the PRM metastases and PRMK tumors were also bound by KMT2C (Fig. 5g). These results strongly suggest that KMT2C directly contributes to the epigenetic reprogramming underlying SCLC metastases.

The resulting transcriptional consequences of KMT2C loss in SCLC cells were revealed by RNA-seq (Extended Data Fig. 7b and Supplementary Table 20). Genes with reduced levels of chromatin accessibility and H3K4me1 were significantly overlapped with those with downregulated expression levels in PRMK cells (Extended Data Fig. 7c,d). Some downregulated genes by *Kmt2c* repression were also frequently mutated in individuals with SCLC (Extended Data Fig. 7d). However, genes with increased H3K4me1 and chromatin accessibility in metastatic SCLC cells were significantly overlapped with those with upregulated levels of H3K4me1 and chromatin accessibility by KMT2C loss (Extended Data Fig. 7e,f); these genes were also upregulated in PRMK tumors compared to in PRM cells (Extended Data Fig. 7g). Of note, the gene signature of KMT2C-deficient SCLC cells was significantly positively enriched in human metastatic SCLC cells (Extended Data Fig. 7h). Thus, KMT2C-loss-induced epigenetic reprogramming could simultaneously down- and upregulate gene expression associated with SCLC metastases. However, there is a remaining paradox of how the loss of KMT2C, an H3K4 methyltransferase

for gene activation, would increase the expression of these metastasis-related genes in SCLC.

KMT2C loss gives rise to global DNA hypomethylation. We noticed that *DNMT3A* was a module 1 gene and was frequently mutated in human SCLC (Extended Data Fig. 3a). It was also among the 106 genes with significantly lower H3K4me1 levels, less chromatin accessibility and lower expression in metastatic SCLC cells than in primary tumor cells (Extended Data Fig. 8a). KMT2C directly bound on multiple regions of the *Dnmt3a* locus, and KMT2C loss reduced binding and H3K4me1 and H3K4me2 levels. These H3K4me1 and H3K4me2 binding sites were overlapped with those of KMT2C binding (Fig. 6a). Similar decreases of KMT2C binding and H3K4me1 level at the same regions were also observed in PRM metastatic tumor cells (Fig. 6a). Accordingly, *Dnmt3a* was progressively downregulated along the metastasis trajectory (Fig. 6b). Consistently, the expression of *Dnmt3a* was significantly repressed by *Kmt2c* disruption in lung organoids and in human SCLC with metastasis compared to those without metastasis (Fig. 6c). In three independent SCLC cohorts, expression of *DNMT3A* was significantly positively correlated with those of *KMT2C* (Extended Data Fig. 8b), and downregulation of *DNMT3A* was associated with poor prognosis of individuals with SCLC (Extended Data Fig. 8c). These data suggest that KMT2C might directly regulate the expression of *DNMT3A* through histone methylation and chromatin remodeling to repress SCLC metastasis.

DNMT3A encodes a de novo DNA methyltransferase, and its loss can lead to global DNA hypomethylation, which is associated with gene activation^{25,26}. Dot blotting showed that the total level of DNA methylation, indicated by 5mC staining, was dramatically reduced in PRMK SCLC compared to in PRM tumors (Fig. 6d). Whole-genome bisulfite sequencing (WGBS) analyses confirmed the reduction of global DNA methylation levels by KMT2C loss in SCLC (Extended Data Fig. 9a). CpG methylation levels, especially those around CpG islands, were reduced in PRMK tumors compared to in PRM tumors (Fig. 6e and Extended Data Fig. 9b). Similar global and CpG DNA hypomethylation was also observed in PRM metastases (Fig. 6f and Extended Data Fig. 9c). In human metastatic SCLC, CpG methylation was reduced compared to in those without metastasis (Extended Data Fig. 9d). Additionally, individuals with SCLC with *KMT2C* mutations also displayed reduced CpG methylation levels compared to those without *KMT2C* mutations (Extended Data Fig. 9e). These data strongly suggest that *KMT2C* deficiency gives rise to DNA hypomethylation in metastatic SCLC in both mouse models and humans.

Consistent with global DNA hypomethylation, differentially methylated region (DMR) analyses showed that there were significantly more hypo-DMRs than hyper-DMRs in PRMK tumors compared to in PRM tumors (Extended Data Fig. 9f and Supplementary Table 21). Similarly, there were more hypomethylated differentially methylated sites in individuals with SCLC with *KMT2C* mutations (Extended Data Fig. 9g and Supplementary Table 22), and 85% of the hypomethylated DMRs were in promoter regions, while only 49% of the hypermethylated DMRs were in promoter regions (Extended Data Fig. 9h). Noticeably, 86.4% of the upregulated genes in PRMK cells displayed DNA hypomethylation, suggesting that DNA hypomethylation is a major mechanism for these upregulated genes for SCLC metastases (Fig. 6g). Genes with DNA hypomethylation were significantly overlapped with those with increased chromatin accessibility and had higher expression levels in PRMK cells than in PRM cells (Extended Data Fig. 9i and Supplementary Table 23). These data suggest that *DNMT3A* deficiency might mediate activation of prometastatic genes in PRMK SCLC.

KMT2C-DNMT3A-MEIS/HOX axis in SCLC metastasis.

DNMT3A has been shown to be a tumor suppressor in leukemia

and non-small cell lung cancer, but its potential function in SCLC, especially metastases, was unknown^{27,28}. *Dnmt3a* overexpression led to a significantly reduced number of PRMK tumor organoids and reduced the formation of axon-like protrusions in PRMK SCLC organoids (Fig. 6h). Fluorescence imaging indicated that forced expression of *Dnmt3a* reduced the growth of PRMK tumors in mice (Fig. 6i). The number of liver metastasis loci in PRMK-*Dnmt3a* mice was significantly less than that observed in PRMK mice (Fig. 6j). CTC frequencies in the peripheral blood of SCLC mice were also significantly reduced by *Dnmt3a* overexpression (Fig. 6k,l and Supplementary Table 24). These results indicate that *DNMT3A* deficiency is a critical mediator of KMT2C loss in SCLC metastasis.

Dnmt3a overexpression increased the level of DNA methylation in PRMK SCLC cells (Extended Data Fig. 9j). *Meis2* was among the common genes with significantly reduced DNA methylation in mouse and human SCLC metastases and tumors with KMT2C loss (Fig. 7a,b) and was one of the top upregulated genes in KMT2C-deficient SCLC with increased chromatin accessibility (Extended Data Fig. 7b,g). MEIS2 is a master regulator and common cotranscription factor of Hox genes, and the promoter regions of multiple Hox genes, including *Hoxb5* and *Hoxb7*, were significantly less methylated in PRMK tumors than in PRM tumors (Fig. 7c) and their expression was significantly upregulated in PRMK tumors compared to in PRM tumors (Fig. 7d). While *Dnmt3a* disruption in PRM SCLC organoids significantly upregulated the expression levels of *Meis2* and multiple *Hoxb* genes, *Dnmt3a* overexpression partially reduced expression levels in PRMK tumor organoids (Fig. 7e,f).

To test the functional roles of *Meis/Hox* genes in SCLC, we disrupted *Meis2* by CRISPR/Cas9 in PRMK SCLC organoids. *Meis2* loss significantly reduced the number of tumor organoids and number of axon-like protrusions in the PRMK organoids compared to scramble sgRNA (Fig. 7g). sg*Meis2* PRMK SCLC grew significantly slower than sgScr PRMK SCLC (Fig. 7h). While all mice with the sgScr PRMK tumor had SCLC metastasis in lymph nodes, liver and other organs, less than half of the mice with the sg*Meis2* PRMK tumor had metastasis, which only happened in the lymph nodes (Fig. 7i). *Meis2* loss downregulated the epithelial–mesenchymal transition gene signature and other genes involved in cell migration in PRMK SCLC cells (Fig. 7j and Supplementary Table 25). Taken together, these data indicate that *Meis2/Hox* genes are important mediators for KMT2C-DNMT3A loss to drive SCLC metastasis.

S-Adenosyl methionine (SAM) treatment for SCLC. Given the critical roles of the concerted histone methylation and DNA methylation, likely driven by *KMT2C* and *DNMT3A* deficiencies, in SCLC metastasis, we looked for treatments that could rescue these epigenetic abnormalities. Thanks to the heterozygous mutations or transcriptional repression of *KMT2C* and *DNMT3A* in most SCLC, we proposed that SAM, the common substrate of histone and DNA methyltransferases, might be a proof-of-concept inhibitor for SCLC metastasis. SAM treatment significantly increased DNA 5mC levels and the levels of H3K4me1 and H3K4me2 in PRMK SCLC cells (Extended Data Fig. 10a,b). Growth of PRMK tumor organoids was significantly inhibited by SAM treatment in a dose-dependent manner (Fig. 8a), and SAM treatment significantly reduced the formation of axon-like protrusions in these organoids (Fig. 8b,c).

Oral administration of SAM restrained the growth of PRMK SCLC in mice, as indicated by reduced fluorescence intensity (Fig. 8d). There were fewer CTCs in the peripheral blood of mice treated with SAM than in the blood of mice treated with vehicle (Fig. 8e and Extended Data Fig. 10c). The numbers of liver metastatic nodules in SAM-treated mice with PRMK SCLC were significantly reduced compared to those observed in vehicle-treated mice, as indicated by GFP⁺ lesions and verified by histological analyses (Fig. 8f-h). Growth of both organoids from two individuals with SCLC was also significantly repressed by SAM in a dose-dependent pattern

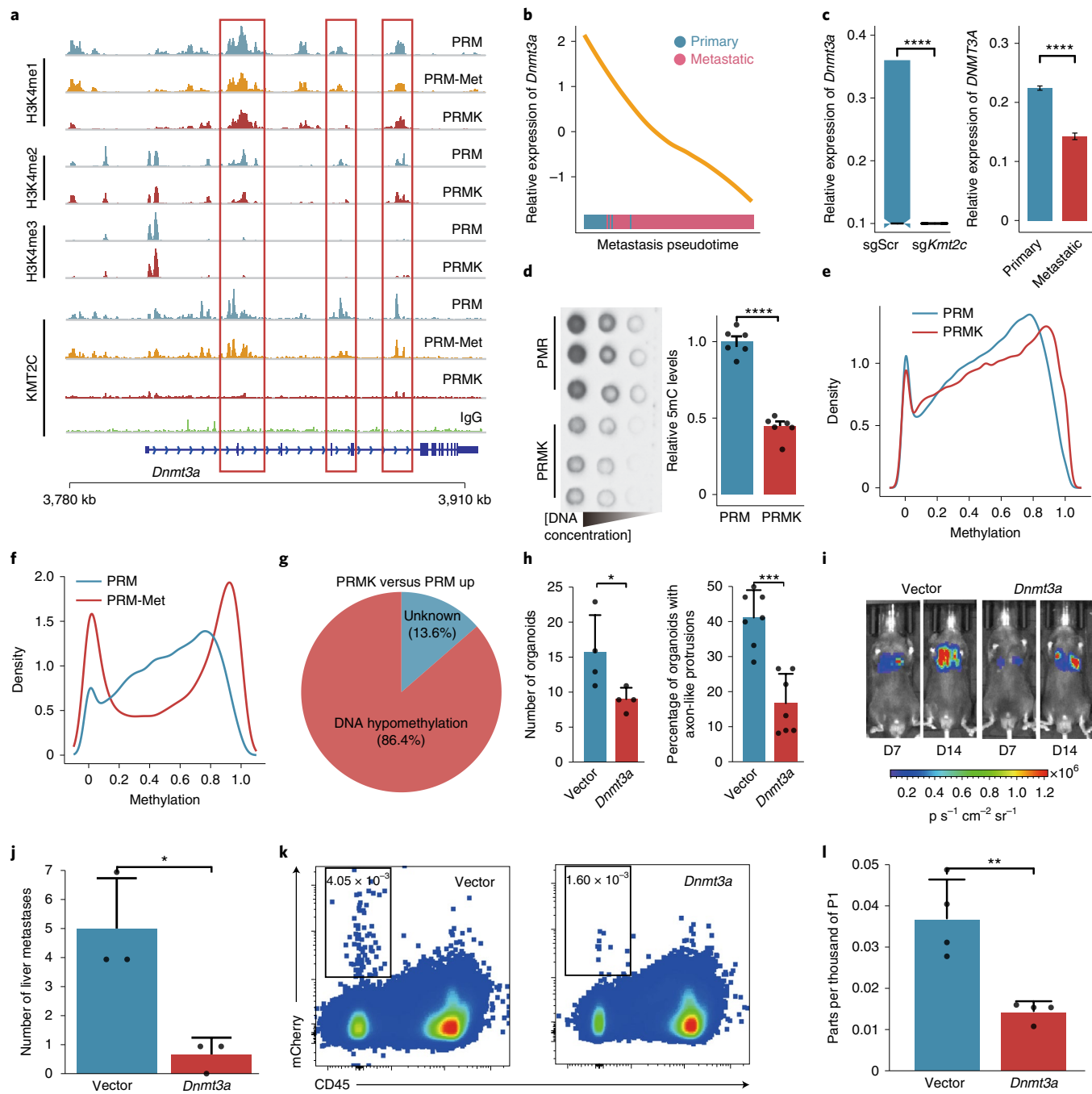


Fig. 6 | DNA hypomethylation mediates the functions of KMT2C deficiency in SCLC metastasis. **a**, IGV plots showing H3K4me1, H3K4me2, H3K4me3 and KMT2C binding density on *Dnmt3a* in PRM, PRM-Met and PRMK cells. The significant variation regions are labeled. **b**, Dynamics of relative expression levels of *Dnmt3a* on metastasis trajectory. **c**, Relative expression levels of *Dnmt3a* in murine sgScr and sgKmt2c lung organoids (left; $n=2,794$ cells sgScr and $n=2,794$ cells sgKmt2c) and human primary and metastatic SCLC cells (right; $n=10,000$ cells primary and $n=2,000$ cells metastatic). Data are shown as mean \pm s.e.m. The box bounds the interquartile range divided by the median, with the whiskers extending to a maximum of 1.5 times the interquartile range beyond the box. The *P* value was calculated by Wilcoxon signed-rank test. **d**, Dot blotting of DNA 5-methylcytosine (5mC) in PRM and PRMK SCLC cells (left). The statistics of DNA 5mC levels in SCLC cells is shown on the right. Data are shown as mean \pm s.e.m.; $n=6$. Significance was calculated by two-sided Student's *t*-test. **e**, Density plot showing methylation levels at CpG sites in PRM and PRMK SCLC cells. **f**, Density plot showing methylation levels of CpG sites in PRM and PRM-Met SCLC cells. **g**, Pie chart showing the concordant percentage of upregulated genes with reduced 5mC levels in PRMK cells compared to PRM cells. **h**, Numbers of organoids (left) and percentages of organoids (right) with axon-like protrusions with empty vector or *Dnmt3a* overexpression. Data are shown as mean \pm s.d.; left, $n=4$; right, $n=7$. Significance was calculated by two-sided Student's *t*-test. **i**, Representative bioluminescence images of mice with PRMK-vector or PRMK-*Dnmt3a* SCLC at days 7 and 14 after transplantation. **j**, Numbers of metastatic lesions in the livers of vector and *Dnmt3a* mice. Data are shown as mean \pm s.d.; $n=3$. Significance was calculated by two-sided Student's *t*-test. **k**, Representative flow cytometry plots showing CD45-mCherry⁺ CTCs in mice with PRMK-vector SCLC or PRMK-*Dnmt3a* SCLC. Data are shown as mean \pm s.d.; $n=4$ mice. Significance was calculated by two-sided Student's *t*-test; * $P<0.05$, ** $P<0.01$, *** $P<0.001$, **** $P<0.0001$.

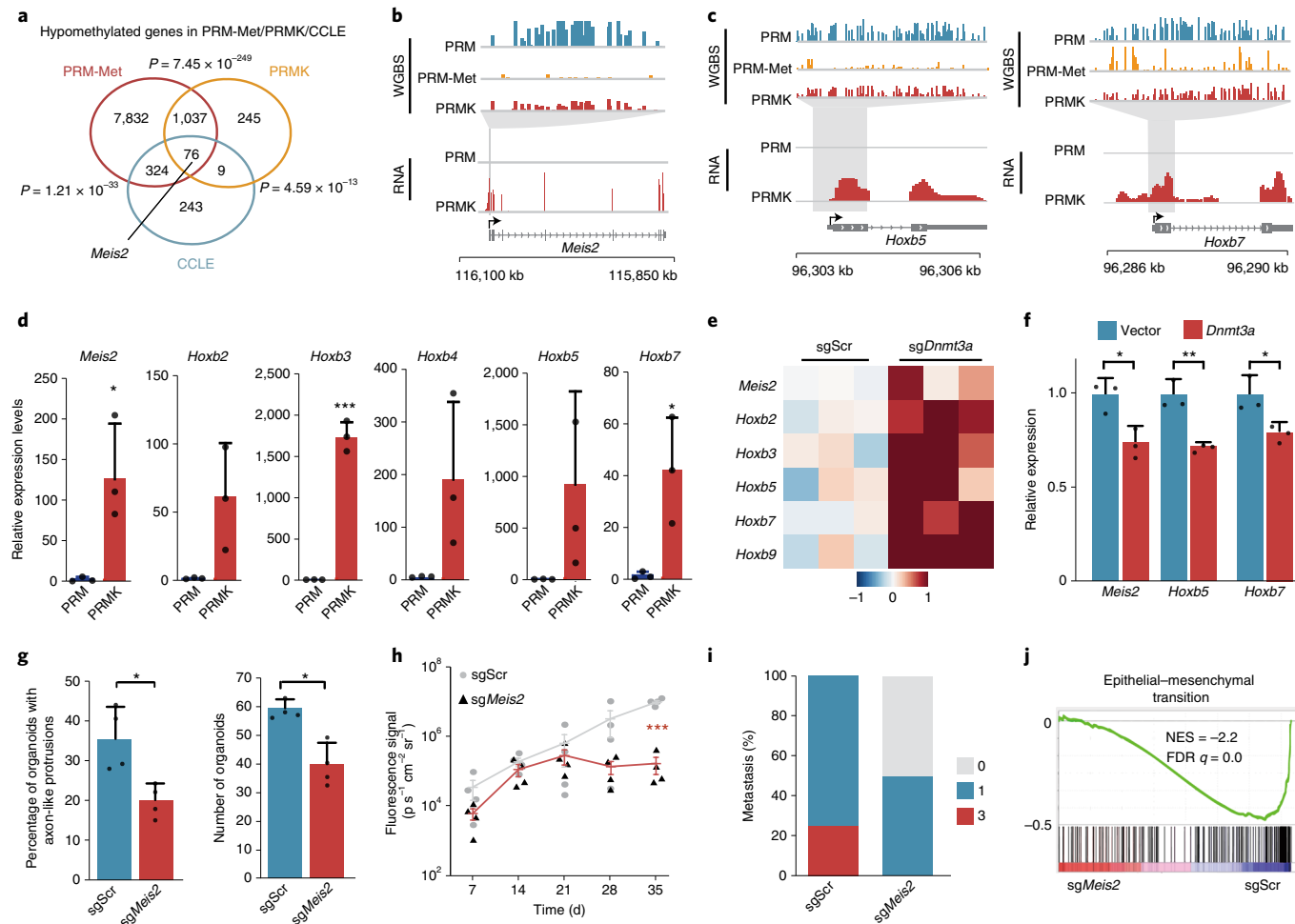


Fig. 7 | Meis/Hox genes are downstream of the KMT2C-DNMT3A epigenetic reprogramming for SCLC metastasis. **a**, Venn diagram showing overlapping of the hypomethylated genes in PRM-Met compared to PRM, PRMK compared to PRM and CCLE KMT2C mutant compared to CCLE KMT2C wild type. *P* values were calculated by a hypergeometric test. **b**, IGV plots showing the 5mC densities and RNA-seq peaks of the *Meis2* gene bodies. **c**, IGV plots showing the 5mC densities and RNA-seq peaks of the *Hoxb5* and *Hoxb7* gene bodies. **d**, Relative expression levels of *Meis2*, *Hoxb2*, *Hoxb3*, *Hoxb4*, *Hoxb5*, and *Hoxb7* in PRM and PRMK tumor organoids, as measured by real-time quantitative PCR (RT-qPCR). Data are shown as mean \pm s.d.; $n=3$ mice. Significance was calculated by two-sided Student's *t*-test. **e**, Relative expression levels of *Meis2*, *Hoxb2*, *Hoxb3*, *Hoxb5*, *Hoxb7* and *Hoxb9* in PRM tumor organoids with sgScr and sg*Dnmt3a*, as measured by RT-qPCR; $n=3$ mice. **f**, Relative expression of *Meis2*, *Hoxb5* and *Hoxb7* in PRMK organoids with vector or *Dnmt3a* overexpression, as measured by RT-qPCR. Data are shown as mean \pm s.d.; $n=3$ organoids. Significance was calculated by two-sided Student's *t*-test. **g**, Percentages of the sgScr and sg*Meis2* PRMK SCLC organoids with axon-like protrusions (left) and the number of total sgScr and sg*Meis2* PRMK organoids (right). Data are shown as mean \pm s.d.; $n=4$. Significance was calculated by two-sided Student's *t*-test. **h**, Luciferase fluorescence signal intensities of mice with sgScr or sg*Meis2* PRMK SCLC. Data are shown as mean \pm s.e.m.; $n=4$ mice. Significance was calculated by two-sided Student's *t*-test. **i**, Percentages of sgScr and sg*Meis2* PRMK mice with the indicated number of metastases. **j**, Gene set enrichment analysis showing negative enrichment of the epithelial-mesenchymal transition gene signature in sg*Meis2* PRMK cells compared to those with sgScr; **P* < 0.05, ***P* < 0.01, ****P* < 0.001; NES, normalized enrichment score; FDR, false discovery rate.

(Fig. 8i). RNA-seq analyses showed that SAM treatment could not only repress pathways related to tumor metastases but also enhance multiple histone and DNA methylation pathways. Genes upregulated by SAM treatment were significantly overlapped with those with reduced histone and DNA hypomethylation in PRMK tumors (Fig. 8j and Supplementary Table 26). These results suggest that SAM treatment could repress SCLC by rescuing histone and DNA epigenetic abnormalities (Extended Data Fig. 10d and Supplementary Table 27).

In summary, our study reveals the critical roles of KMT2C in SCLC metastasis. We find that KMT2C loss leads to concordant histone and DNA hypomethylation, which simultaneously represses antimetastasis genes and activates prometastasis genes, including *MEIS2* and *HOX* genes, respectively, and thus suggests susceptibilities for this disease (Fig. 8k).

Discussion

Despite metastasis being the leading cause of death for individuals with cancer, so far, there have been very few driver mutations identified for metastasis⁴. With our models, we find that KMT2C deficiency is a major driver for SCLC metastasis. KMT2C is frequently mutated in many human cancers²⁹. Previously, we have reported that its haploinsufficiency promotes leukemogenesis through repressing differentiation-related genes²². However, its role in solid cancers remains unknown. In this study, we demonstrate that KMT2C is a bona fide tumor suppressor gene (TSG) in SCLC. The functional roles of KMT2C in metastasis were validated with multiple ex vivo and in vivo models. Our work not only validates KMT2C as a TSG in SCLC but also reveals KMT2C as a driver for metastasis. Several other KMT2C-related epigenetic regulators, such as KMT2D and

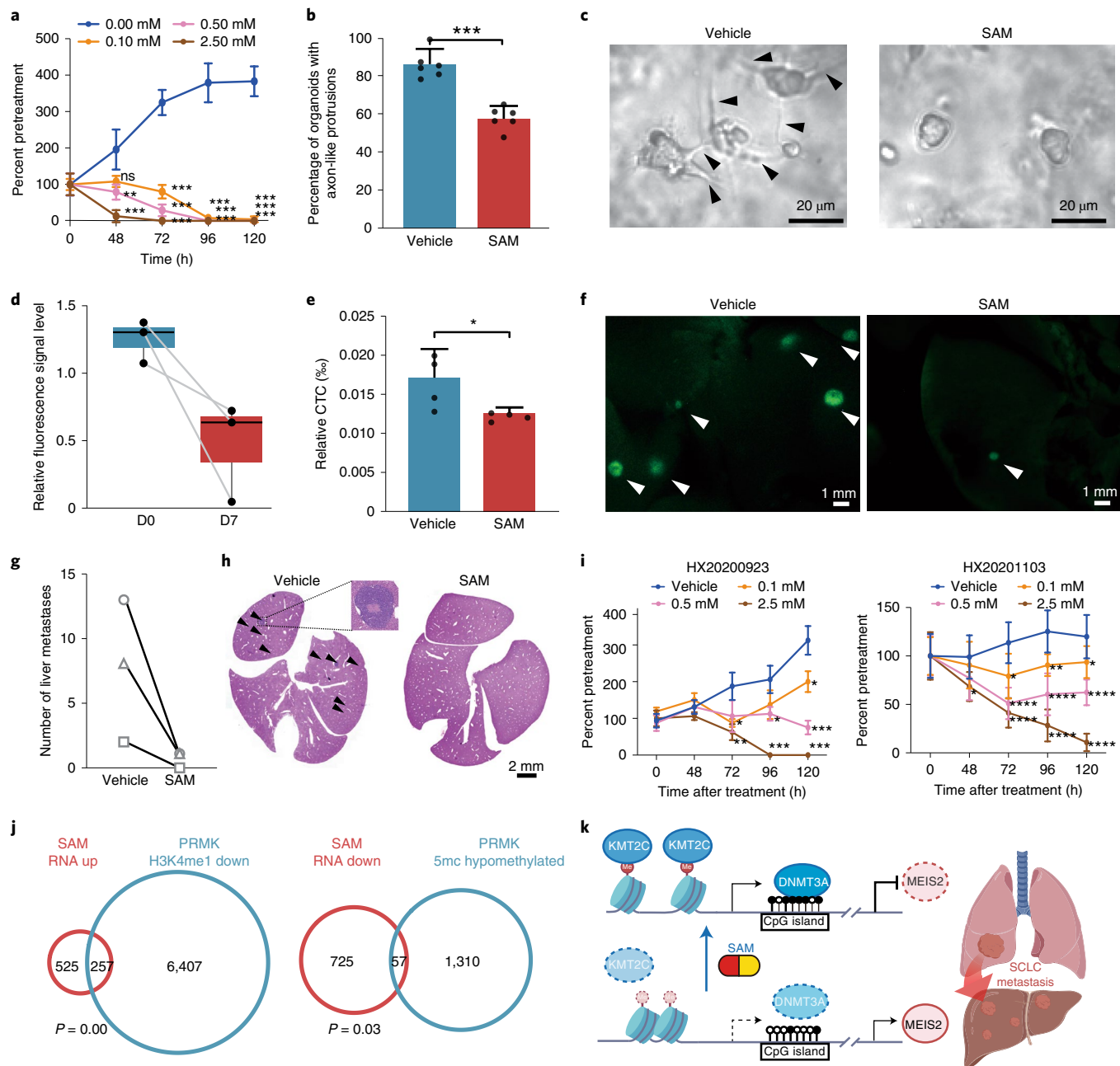


Fig. 8 | SAM treatment reversed both H3K4 and DNA hypomethylation in KMT2C-deficient SCLC and restrained metastasis. **a**, Growth curves of PRMK organoids treated with vehicle or SAM at the indicated concentrations over time. Data are shown as mean \pm s.d.; $n=3$ experiments. Significance was calculated by two-sided Student's *t*-test. **b**, Percentages of PRMK SCLC organoids with axon-like protrusions after treatment with vehicle or 0.02 mM SAM. Data are shown as mean \pm s.d.; $n=6$ experiments. Significance was calculated by two-sided Student's *t*-test. **c**, Representative brightfield images of PRMK SCLC organoids treated with vehicle ($n=5$) or SAM ($n=5$). **d**, Relative luciferase fluorescence signal intensities (SAM versus vehicle) of three pairs of SCLC mice at day 0 (D0) and day 7 (D7) after SAM or vehicle treatments. The box bounds the interquartile range divided by the median. **e**, Percentages of CTCs in SCLC treated with vehicle or SAM. Data are shown as mean \pm s.d.; $n=4$ mice. Significance was calculated by two-sided Student's *t*-test. **f**, Representative fluorescence images of liver tissue from mice with PRMK SCLC treated with vehicle (left) or SAM (right); $n=3$ mice. **g**, Number of metastatic liver lesions in the livers of three pairs of PRMK SCLC mice treated with vehicle or SAM at the end of treatments. **h**, Representative H&E staining of liver sections of PRMK SCLC mice treated with vehicle or SAM. **i**, Growth curves of SCLC organoids from two individuals treated with vehicle and SAM at the indicated concentrations over time. Data are shown as mean \pm s.d.; three independent repeats were performed. Significance was calculated by two-sided Student's *t*-test. **j**, Left, Venn diagram showing overlapping of the upregulated genes in SAM-treated PRMK SCLC cells compared to those treated with vehicle and H3K4me1 downregulated genes in PRMK cells. Right, Venn diagram showing overlapping of the downregulated genes in SAM-treated PRMK SCLC cells compared to those treated with vehicle and hypomethylated genes in PRMK cells compared to PRM cells. The *P* values were calculated by a hypergeometric test. **k**, Working model for KMT2C in SCLC tumorigenesis and metastasis; **P* < 0.05, ***P* < 0.01, ****P* < 0.001, *****P* < 0.0001.

KDM6A, are also frequently mutated in SCLC. *KMT2C* shares the same COMPASS-like complex and has been shown to be a TSG in non-small cell lung cancer³⁰. Whether these genes have similar functions in the tumorigenesis and metastasis of SCLC needs further study. Additionally, it would be interesting to test whether *KMT2C* and its related genes play significant roles in metastases of other cancers.

KMT2C is an H3K4 methyltransferase and is associated with gene activation³¹; therefore, it is expected that downregulation of the majority of downstream genes of *KMT2C* in acute myeloid leukemia with *KMT2C* loss is observed³². However, in SCLC, we find that *KMT2C* deficiency not only represses the expression of metastasis-associated TSGs but also upregulates metastasis-promoting genes, such as *MEIS2* and several *HOXB* genes. *MEIS/HOX* genes are overexpressed in human SCLC, and overexpression occurs in the metastasis of various types of cancer^{32,33}. We show that DNA hypomethylation, mediated by downregulation of *DNMT3A*, a direct target of *KMT2C*, underlies activation of these prometastatic genes. Our study provides an example of how an epigenetic regulator coordinates the expression of genes with opposite functions (here pro- and antimetastasis) through concerted epigenetic reprogramming. Consistently, it has been shown that epigenetic reprogramming, but not genetic mutations, is associated with metastasis³⁷. *FOXA1*-mediated enhancer activation can drive the progression and metastasis of pancreatic cancer³⁴. These data strongly suggest that epigenetic reprogramming might be a major driver of cancer metastasis and potential other hallmarks³⁵.

The unexpected link between *KMT2C* loss-initiated histone and DNA hypomethylation and metastasis might have broad implications. A global increase of chromatin accessibility driven by *NFIB* can explain metastasis in some individuals with SCLC^{13,14}. Here, an opposite chromatin status associated with decreased H3K4 methylation suggests a potential molecular mechanism for SCLC metastasis, which is consistent with the emerging concept that SCLC is a highly heterogeneous disease^{15,36,37}. The paradoxical epigenetic patterns in *NFIB*- and *KMT2C*-loss-driven SCLC reflect the complexity of epigenetic ‘drivers’ for metastasis in human cancers^{38,39}. The putative inter- and intraheterogeneity of metastases remains unexplored and might become a challenge for potential treatment.

Our findings demonstrating prometastatic histone and DNA hypomethylation could provide treatment options for SCLC. Epigenetic drugs, such as 5-azacytidine, histone deacetylase inhibitors and EZH2 inhibitors, have been approved for cancer treatment. SAM is an approved clinical drug for liver cirrhosis, depressive disorder, osteoarthritis and other syndromes. Treatment with SAM, the common cofactor for many methyltransferases, can enhance both H3K4 and DNA methylation, potentially through *KMT2C* (in those without homozygous loss), *DNMT3A* and others, and thus impairs the metastatic capacity of SCLC. This kill-two-birds-with-one-stone strategy might be a promising therapy for this recalcitrant malignancy. It has been reported that EZH2 overexpression underlies SCLC chemoresistance⁴⁰. EZH2 is responsible for H3K27 methylation, which can be antagonized by *KDM6A*, an H3K27 demethylase and a component of the COMPASS-like complex with *KMT2C*. Inhibition of LSD1, an H3K4 and H3K9 demethylase, can repress SCLC with DNA hypomethylation^{41,42}. These data are consistent with our observation that *KMT2C* deficiency promotes histone and DNA hypomethylation-associated malignancy. It would be interesting to test whether *KMT2C* is also involved in chemotherapy treatment response and, on the other hand, whether EZH2 and LSD1 inhibitors would restrain metastasis of SCLC.

Methods

This study complied with all relevant ethical regulations and was approved by the Ethics Committee on Biomedical Research, West China Hospital of Sichuan University. Written informed consent was provided by all participants.

Mice. Mice were kept in the specific pathogen-free animal facility in Sichuan University with autoclaved food, bedding and water. Animals were housed at room temperature ($23 \pm 2^\circ\text{C}$) at a humidity of 30–70% on a 12-h light/12-h dark cycle (6:00–18:00). All mouse experiments were performed in compliance with the Guide for the Care and Use of Laboratory Animals of Sichuan University and were approved by the Animal Care and Use Committee of Sichuan University. C57BL/6 (Jackson Laboratories, 000664) and CAG-Cas9-EGFP mice (Jackson Laboratories, 026179) (male, 8–10 weeks old and ~20 g weight) were used. Mice were monitored for tumorigenesis by bioluminescent imaging and micro-CT scans. In our mouse experiments, the tumor volumes did not exceed the maximal permitted tumor volume of 1,000 mm³.

Cell culture. HEK 293T cells (CRL-1573) were from ATCC and were cultured at 37 °C with 5% CO₂ in DMEM supplemented with 10% (vol/vol) fetal bovine serum and penicillin (100 U ml⁻¹)/streptomycin (0.1 mg ml⁻¹). The HEK 293T cell line was routinely tested for mycoplasma by PCR. Experiments were performed within 4 weeks after fresh viable cells were thawed.

Lung organoid culture. Mouse lungs were removed, flushed, cut into 5-mm³ pieces and incubated with digestion buffer containing 1.0 mg ml⁻¹ collagenase I (Gibco, 17100-017) and 0.5 mg ml⁻¹ collagenase IV (Gibco, 17104-019) in DMEM/F12 (Gibco, C11330500B) in gentleMACS C tubes (Miltenyi Biotec, 130-096-334). After dissociation by the gentleMACS dissociator, samples were filtered through 70-μm filters, collected by centrifugation and resuspended in ice-cold Matrigel (BD, 354230) at a ratio of 1:20 (vol:vol). The basic culture medium for mouse lung organoids was slightly modified from a previous report⁴³, where DMEM/F12 was supplemented with penicillin/streptomycin (Gibco, 15140-122), 2 mM GlutaMAX (Peprotech, 35050-061), 1X B27 (Gibco, A3582801), 1X N2 (Gibco, 17502048), 10 nM gastrin I (Peprotech, 1003377), 1 mM N-acetylcysteine (Sigma, A9165) and 10 mM nicotinamide (Sigma, N0636). The following growth factors were used: 50 ng ml⁻¹ mouse recombinant epidermal growth factor (Peprotech, AF-100-15-1000), 100 ng ml⁻¹ mouse recombinant noggin (Peprotech, 120-10C-250), 500 ng ml⁻¹ mouse recombinant FGF10 (Peprotech, 100-26-1000), 125 ng ml⁻¹ R-spondin-1 (Peprotech, 120-38-1000), 10% Wnt-3A conditioned medium and 500 nM A83-01 (Peprotech, 9094360). The medium was changed every 3 d. Organoids were passaged by mechanical dissociation in TrypLE (Gibco, 12605-028) every 5–7 d.

Organoid genome editing. sg*Kmt2c* was the same as was used in our previous report⁴². sgRNAs (Supplementary Table 28) were designed with the CRISPR Design Tool (<http://crispr.mit.edu/>) and cloned into the lentiviral vector V2TC, which bicistronically expresses sgRNA and mCherry. After organoid dissociation with TrypLE, cells were mixed with lentivirus and centrifuged for 1 h at 787*g* and incubated for 1.5 h at 37 °C. Cells were resuspended in ice-cold Matrigel. To validate targeted mutations, genomic DNA was isolated from infected organoids, and the T7E1 (Vazyme, EN303-01) assay was performed with the PCR product for each sgRNA.

Organoid orthotopic transplantation. Organoid fragments were prepared through digestion in TrypLE at 37 °C followed by mechanical disassociation, centrifugation and resuspension in 30% Matrigel. After induction of anesthesia, the left thorax of the recipient mice was shaved and sterilized. A 0.5-cm flank incision was made to expose the intercostal muscle. Then, 300,000 cells in a 0.075-ml volume were injected into the left lobe of the lung within 10 s.

Micro-CT and bioluminescent imaging. Mice were scanned for 340 s under isoflurane anesthesia using a small animal Quantum FX Micro-CT (PerkinElmer) at 45-mm resolution and 90 kV with a 160-mA current. Images were acquired and analyzed with PerkinElmer Quantum FX software. For bioluminescent imaging, mice were given 150 mg kg⁻¹ d-luciferin potassium salt (Biovision, 7903-10PK) intraperitoneally and imaged on the IVIS Spectrum In Vivo Imaging system (PerkinElmer).

In vitro and in vivo treatment. SAM (Sigma, A7007) was added at the indicated concentrations into three replicate wells with tumor organoids. Organoids were counted at 48, 72, 96 and 120 h after treatment. For in vivo treatment, approximately 2×10^6 PRMK cells were injected into the left lungs of 8-week-old C57BL/6 mice. Mice were monitored for tumor burden by bioluminescence. SAM treatment was initiated at 12 d after transplantation. Mice were treated with 100 mg kg⁻¹ every day for 14 d with SAM or vehicle by gavage. Mice were killed and analyzed once moribund or at the indicated time points.

Whole-mount immunostaining and IHC staining. Isolated tumor tissues were immediately fixed with 4% paraformaldehyde overnight. Paraffin-embedded tissues were cut at 4 μm and stained for IHC. Organoids were fixed by adding 300 μl of 4% paraformaldehyde per well and incubating overnight for whole-mount immunostaining. Primary antibodies were applied at 1:50–1:500 dilutions in 2% goat serum and incubated overnight at 4 °C. A two-step detection kit (ZSGB-BIO, PV-9001 and PV-9002) was used for IHC and hematoxylin for nuclear staining.

For whole-mount immunostaining, fluorescence-conjugated secondary antibodies were used.

Western blotting. Histone methylation western blotting was done with acid extracts from organoids. The following antibodies were used: H3K4me1 (Abcam, ab8895, 1:2,000), H3K4me2 (Abcam, ab7766, 1:2,000), H3K4me3 (Abcam, ab8580, 1:1,000), H3K9me3 (Abcam, ab8898, 1:2,000), H3K27me3 (Cell Signaling, 9733S, 1:1,000), H3K27ac (Abcam, ab4729, 1:2,000), H3K36me3 (Cell Signaling, 4909S, 1:1,000), KMT2C (Abcam, 71200, 1:400) and H3 (Hangzhou HuaAn Biotechnology, EM30605, 1:3,000).

RNA extraction and RT-qPCR. Total RNA was extracted with TRIzol (Applied Biosystems, 15596026) following the manufacturer's instructions. M-MLV reverse transcriptase (Invitrogen, 28025013) was used for reverse transcription according to the manufacturer's protocol. RT-qPCR was performed using Powerup SYBR Green master mix (Applied Biosystems, A25741) in QuantStudio 3 (Applied Biosystems). The relative expression of genes was calculated using the $2^{-\Delta\Delta C_t}$ method. Gene expression was normalized to that of *Actb* or *Hprt*. RT-qPCR was performed on each sample in triplicate. Primer sequences were used to amplify mouse *Meis2*, *Hoxb2*, *Hoxb3*, *Hoxb4*, *Hoxb5*, *Hoxb7*, *Hoxb9*, *Ascl1*, *Ncam1*, *Syp* and *Chga* are listed in Supplementary Table 29.

Flow cytometry. Peripheral blood was obtained from retro-orbital puncture, and red blood cells were lysed by ACK lysis buffer. CD45 (BioLegend, 109820, 1:200) staining was performed at 4°C for 30 min. Flow cytometry analysis was performed on Fortessa machines (BD Bioscience), and data were analyzed with FlowJo.

DNA 5mC dot blotting assay. Dot blotting was performed as described in ref.⁴⁴. Briefly, purified genomic DNA was quantified on a NanoDrop and denatured by 0.1 M NaOH. Serial-diluted DNA was spotted on a nitrocellulose membrane. 5mC antibody (Active Motif, 39649, 1:3,000) was used.

RNA-seq analyses. RNA-seq libraries were constructed using an Illumina stranded mRNA sample preparation kit (NEB, E7770) according to the manufacturer's protocol and were sequenced on an Illumina NovaSeq 6000 sequencing machine with 150-base pair (bp) paired-end reads. The RNA-seq reads were aligned to the mouse reference genome (GRCm38) by STAR_2.6.0a. Transcript abundance was normalized and measured by transcripts per kilobase million. DESeq2 (v.1.26.0, RRID:SCR_000154) was used to identify differentially expressed genes. Genes with an absolute fold change greater than 0.5 and a *P* value of <0.05 were counted as differentially expressed genes. Pheatmap (v.1.0.12, RRID:SCR_016418) was used to display heat maps of the expression levels of differentially expressed genes, which were normalized by *z* score.

WGBS analyses. WGBS libraries were prepared with an EZ DNA Methylation-Gold kit (Zymo Research, D5005) and VAHTS Universal DNA library prep kit (Vazyme, ND607). Sequencing was performed on an Illumina NovaSeq instrument, and reads were aligned to mm10 by BS-Seeker2 (v.2.1.8) with Bowtie 2 aligner. To remove PCR duplicates, MarkDuplicates, implemented in GATK (v.4.1.3), was used with -REMOVE_DUPLICATES=true. Bismark (v.0.22.3) was used for methylated site calling. Differentially methylated site analysis and annotation were performed by the R package methylKit (v.1.12.0). The program metilene (v.0.2.7) was used to identify DMRs based on analyzing the raw methylation ratios at all CpGs. ViewBS (v.0.1.9) was used to draw the methylation levels over regions. IGV (v.2.7.0) was used to visualize the methylation levels.

ATAC-seq analyses. Library preparation was performed as previously described⁴⁵. The library was sequenced on an Illumina NovaSeq 6000 sequencing machine with 150-bp paired-end reads. NGmerge (v.0.3) was used to remove the adapters from the raw data. Bowtie2 (v.2.2.1) was used to align reads to the mm10 genome, and Samtools (v.1.8) was used to generate the .bam files. MarkDuplicates, implemented in GATK (v.4.1.3), was used with -REMOVE_DUPLICATES=true to remove the PCR duplicates. Bigwig files were generated by bamCoverage with bins per million normalizing to remove library size effects. For optimizing peak calling in ATAC-seq data, HMMRATAC (v.1.2.5) was used as the peak detector to call peak regions in each sample. Heat maps and average profiles of ATAC-seq peaks were generated with Deeptools (v.3.5.1, RRID:SCR_016366). ChiPseeker (v.1.22.1) was used to annotate the regions in each peak, and global TSS distribution was annotated by using TxDb.Mmusculus.UCSC.mm10.knownGene as the reference genome in R (v.3.6.1). FeatureCounts (RRID:SCR_012919) was used to quantify the count levels in each peak region. The DESeq2 (v.1.26.0, RRID:SCR_000154) pipeline was used to detect the significantly differentially expressed peaks, with a *P* value of <0.05 and |log₂ fold change| of >0.5.

CUT&Tag analyses. The CUT&Tag assay was performed using a NovoNGS CUT&Tag 2.0 High-Sensitivity kit (Novoprotein Scientific, N259-YH01-01A). Sequencing was performed on an Illumina NovaSeq 6000 with 150-bp paired-end reads, and reads were mapped to mm10 with Bowtie 2 (v.2.3.4.2) with the following options: -local -very-sensitive -no-mixed -no-discordant -phred33 -I 10 -X 700.

MarkDuplicates, implemented in GATK (v.4.1.3), was used with -REMOVE_DUPLICATES=true to remove the PCR duplicates. SEACR (v.1.3) was used for peak calling. Differential histone modification analysis (H3K4me1, H3K4me2 and H3K4me3) was performed by diffReps (v.1.55.6, RRID:SCR_010873), and differential histone modification analysis (KMT2C) was performed with DESeq2 (RRID:SCR_000154). The R package ChiPseeker (v.1.22.1) was used to annotate peak regions. Bigwig files were generated from .bam files with Deeptools (v.3.5.1, RRID:SCR_016366) with bins per million normalization. IGV was used for peak visualization. Visualization of the average profile of CUT&Tag peaks was performed with Deeptools (v.3.5.1, RRID:SCR_016366). The following antibodies were used for CUT&Tag: H3K4me1 (Abcam, ab8895, 1:50), H3K4me2 (Abcam, ab7766, 1:50), H3K4me3 (Abcam, ab8580, 1:50) and KMT2C (Abcam, 71200, 1:50).

scRNA-seq analyses. Libraries were prepared using Chromium Single Cell 3' Reagent kits v.2 according to the manufacturer's protocol (10x Genomics) and were sequenced using an Illumina NovaSeq 6000 platform. Exogenous sequences (the constructs for expressing sgRNAs and *Myc*) were added to the reference genome to distinguish tumor and non-tumor cells. CellRanger (v.2.1.1) was used to align clean reads with mm10. The Seurat (v.3.2.0) pipeline was applied to the analysis to visualize the scRNA-seq data. Genes expressed in less than three cells were not considered, and cells that had mitochondrial ratios lower than 10% and that expressed at least 200 but not more than 6,000 genes were retained for analysis.

All data sets were merged by the Seurat function 'merge', and 4,000 variable genes identified by 'vst' mode were used to calculate the principal components analysis. t-SNE, UMAP and PHATE were used to reduce dimensions by considering 30 principal components. Slingshot (v.1.4.0) was used to construct the development tree and calculate the pseudotime. Dynamically expressed genes were identified by the VGAM function with a full model of 'sm.ns(Pseudotime)', and *q* values higher than 10×10^{-50} were filtered. Dynamically expressed gene modules were identified by calculating the distance of gene–gene Pearson correlation coefficient in Monocle2 packages (v.2.14.0). Expression patterns were visualized with the pheatmap (v.1.0.12, RRID:SCR_016418) package, and enrichGO, implemented in clusterProfiler (v.3.14.3, RRID:SCR_016884), was used to enrich the Gene Ontology biological process in each module.

Gene signature calculation. The CCLE SCLC metastasis signature was calculated from the CCLE SCLC database with relative expression levels of >0.5 and *P*<0.05 by *t*-test. The CDX SCLC metastasis signature was calculated from the human CTC scRNA-seq data²⁰ with relative expression levels of >0.1 and *P*<0.05 by Wilcoxon rank-sum test. The murine SCLC metastasis signature was defined by the Seurat function FindAllMarkers with default parameters. Genes specifically upregulated in metastatic cells with adjusted *P* values of <0.05 and pct.2<0.6 were included (pct.2 is a FindAllMarkers parameter and means the percentage of cells where the gene is detected in the second group).

Statistics and reproducibility. RT-qPCR, organoid diameter and number assays, tumor measurements, metastasis diameter and number assays, CTC assays, 5mC quantification and in vitro treatment were analyzed for statistical significance using two-sided unpaired parametric Student's *t*-tests (Prism 8.0, GraphPad software). Statistical significance was denoted as **P*<0.05, ***P*<0.01, ****P*<0.001 and *****P*<0.0001. The data distribution was assumed to be normal, but this was not formally tested. The numbers of independent experiments, samples or events are indicated in the figure legends. For in vivo treatment experiments, the treatment and vehicle groups were randomized according to their tumor burden before treatment. For in vitro treatment experiments, all samples were randomly assigned to vehicle or treatment groups. Tumor measurements were performed blindly. Measurements of organoid shapes and the number of metastases were analyzed blindly. For other in vivo and in vitro experiments, researchers were not blinded while performing the experiments. No statistical methods were used to predetermine sample sizes, but our sample sizes are similar to those reported in previous publications⁴⁶. No data were excluded from the study.

The statistical power of the expression levels on scRNA-seq data was calculated by a Wilcoxon rank-sum test. All the error bars of omics bar plots represent s.e.m. All statistical powers of Venn plots were calculated by a hypergeometric test. All statistical powers of Kaplan–Meier survival curves were calculated by log-rank test. All quantification and visualization of omics data were performed on R v.3.6.

Reporting Summary. Further information on research design is available in the Nature Research Reporting Summary linked to this article.

Data availability

The RNA-seq, ATAC-seq, CUT&Tag, WGBS and scRNA-seq data in this study are deposited in the NCBI Gene Expression Omnibus under accession number GSE161570. The processed files for omics analysis were submitted to the Figshare database (https://figshare.com/articles/dataset/A_Coherent_Histone_and_DNA_Hypomethylation_Reprogramming_Drives_Small_Cell_Lung_Cancer_Metastasis/13206338). The SCLC genomics data were downloaded from cBioPortal (<https://www.cbioportal.org/>). The omics data of 39 SCLC cell lines were accessed

from the CCLE database of the depmap portal (<https://depmap.org/portal>), including the mutation, CpG methylation, RNA-seq and annotation information. The RNA-seq data and clinical data of 81 individuals with SCLC were downloaded from ref.²¹. The RNA-seq data of 86 individuals with SCLC were downloaded from ref.⁴⁷. The RNA-seq data of 120 SCLC CDX samples were downloaded from ref.⁴⁸ (<https://doi.org/10.5281/zenodo.3574846>). The scRNA-seq data of individuals with SCLC were downloaded from ref.²⁰. Source data are provided with this paper. All other data supporting the findings of this study are available from the corresponding author on reasonable request.

Code availability

The analysis code can be found at GitHub (<https://github.com/pangxueyu233/KMT2C-in-SCLC-Metastasis>).

Received: 23 June 2021; Accepted: 10 March 2022;

Published online: 21 April 2022

References

1. Valastyan, S. & Weinberg, R. A. Tumor metastasis: molecular insights and evolving paradigms. *Cell* **147**, 275–292 (2011).
2. Hu, Z., Li, Z., Ma, Z. & Curtis, C. Multi-cancer analysis of clonality and the timing of systemic spread in paired primary tumors and metastases. *Nat. Genet.* **52**, 701–708 (2020).
3. Reiter, J. G. et al. Minimal functional driver gene heterogeneity among untreated metastases. *Science* **361**, 1033–1037 (2018).
4. Makohon-Moore, A. P. et al. Limited heterogeneity of known driver gene mutations among the metastases of individual patients with pancreatic cancer. *Nat. Genet.* **49**, 358–366 (2017).
5. Ramaswamy, S., Ross, K. N., Lander, E. S. & Golub, T. R. A molecular signature of metastasis in primary solid tumors. *Nat. Genet.* **33**, 49–54 (2003).
6. van 't Veer, L. J. et al. Gene expression profiling predicts clinical outcome of breast cancer. *Nature* **415**, 530–536 (2002).
7. McDonald, O. G. et al. Epigenomic reprogramming during pancreatic cancer progression links anabolic glucose metabolism to distant metastasis. *Nat. Genet.* **49**, 367–376 (2017).
8. Gazdar, A. F., Bunn, P. A. & Minna, J. D. Small-cell lung cancer: what we know, what we need to know and the path forward. *Nat. Rev. Cancer* **17**, 725–737 (2017).
9. Matthews, M. J., Kanhouwa, S., Pickren, J. & Robinette, D. Frequency of residual and metastatic tumor in patients undergoing curative surgical resection for lung cancer. *Cancer Chemother. Rep.* **34**, 63–67 (1973).
10. H.R.733—Recalcitrant Cancer Research Act of 2012 (US Congress, 2012); <https://www.congress.gov/bill/112th-congress/house-bill/733>
11. Augustyn, A. et al. ASCL1 is a lineage oncogene providing therapeutic targets for high-grade neuroendocrine lung cancers. *Proc. Natl Acad. Sci. USA* **111**, 14788–14793 (2014).
12. Osborne, J. K. et al. NeuroD1 regulates survival and migration of neuroendocrine lung carcinomas via signaling molecules TrkB and NCAM. *Proc. Natl Acad. Sci. USA* **110**, 6524–6529 (2013).
13. Semenova, E. A. et al. Transcription factor NFIB is a driver of small cell lung cancer progression in mice and marks metastatic disease in patients. *Cell Rep.* **16**, 631–643 (2016).
14. Denny, S. K. et al. NFIB promotes metastasis through a widespread increase in chromatin accessibility. *Cell* **166**, 328–342 (2016).
15. Yang, D. et al. Intertumoral heterogeneity in SCLC is influenced by the cell type of origin. *Cancer Discov.* **8**, 1316–1331 (2018).
16. Meuwissen, R. et al. Induction of small cell lung cancer by somatic inactivation of both Trp53 and Rb1 in a conditional mouse model. *Cancer Cell* **4**, 181–189 (2003).
17. Schaffer, B. E. et al. Loss of p130 accelerates tumor development in a mouse model for human small-cell lung carcinoma. *Cancer Res.* **70**, 3877–3883 (2010).
18. Rudin, C. M. et al. Molecular subtypes of small cell lung cancer: a synthesis of human and mouse model data. *Nat. Rev. Cancer* **19**, 289–297 (2019).
19. Ghandi, M. et al. Next-generation characterization of the Cancer Cell Line Encyclopedia. *Nature* **569**, 503–508 (2019).
20. Stewart, C. A. et al. Single-cell analyses reveal increased intratumoral heterogeneity after the onset of therapy resistance in small-cell lung cancer. *Nat. Cancer* **1**, 423–436 (2020).
21. George, J. et al. Comprehensive genomic profiles of small cell lung cancer. *Nature* **524**, 47–53 (2015).
22. Chen, C. et al. MLL3 is a haploinsufficient 7q tumor suppressor in acute myeloid leukemia. *Cancer Cell* **25**, 652–665 (2014).
23. Hodgkinson, C. L. et al. Tumorigenicity and genetic profiling of circulating tumor cells in small-cell lung cancer. *Nat. Med.* **20**, 897–903 (2014).
24. Yang, D. et al. Axon-like protrusions promote small cell lung cancer migration and metastasis. *eLife* **8**, e50616 (2019).
25. Zhang, Z. M. et al. Structural basis for DNMT3A-mediated de novo DNA methylation. *Nature* **554**, 387–391 (2018).
26. Jia, D., Jurkowska, R. Z., Zhang, X., Jeltsch, A. & Cheng, X. Structure of Dnmt3a bound to Dnmt3L suggests a model for de novo DNA methylation. *Nature* **449**, 248–251 (2007).
27. Gao, Q. et al. Deletion of the de novo DNA methyltransferase *Dnmt3a* promotes lung tumor progression. *Proc. Natl Acad. Sci. USA* **108**, 18061–18066 (2011).
28. Mayle, A. et al. Dnmt3a loss predisposes murine hematopoietic stem cells to malignant transformation. *Blood* **125**, 629–638 (2015).
29. Kandoth, C. et al. Mutational landscape and significance across 12 major cancer types. *Nature* **502**, 333–339 (2013).
30. Alam, H. et al. KMT2D deficiency impairs super-enhancers to confer a glycolytic vulnerability in lung cancer. *Cancer Cell* **37**, 599–617 (2020).
31. Shilatifard, A. The COMPASS family of histone H3K4 methylases: mechanisms of regulation in development and disease pathogenesis. *Annu. Rev. Biochem.* **81**, 65–95 (2012).
32. Paco, A., Aparecida de Bessa Garcia, S., Leitao Castro, J., Costa-Pinto, A. R. & Freitas, R. Roles of the HOX proteins in cancer invasion and metastasis. *Cancers* **13**, 10 (2020).
33. Tiberio, C. et al. HOX gene expression in human small-cell lung cancers xenografted into nude mice. *Int. J. Cancer* **58**, 608–615 (1994).
34. Roe, J. S. et al. Enhancer reprogramming promotes pancreatic cancer metastasis. *Cell* **170**, 875–888 (2017).
35. Hanahan, D. Hallmarks of cancer: new dimensions. *Cancer Discov.* **12**, 31–46 (2022).
36. Rudin, C. M., Brambilla, E., Faivre-Finn, C. & Sage, J. Small-cell lung cancer. *Nat. Rev. Dis. Primers* **7**, 3 (2021).
37. Drapkin, B. J. & Rudin, C. M. Advances in small-cell lung cancer (SCLC) translational research. *Cold Spring Harb. Perspect. Med.* **11**, a038240 (2020).
38. Chatterjee, A., Rodger, E. J. & Eccles, M. R. Epigenetic drivers of tumorigenesis and cancer metastasis. *Semin. Cancer Biol.* **51**, 149–159 (2018).
39. Fares, J., Fares, M. Y., Khachfe, H. H., Salhab, H. A. & Fares, Y. Molecular principles of metastasis: a hallmark of cancer revisited. *Signal Transduct. Target. Ther.* **5**, 28 (2020).
40. Gardner, E. E. et al. Chemosensitive relapse in small cell lung cancer proceeds through an EZH2–SLFN11 axis. *Cancer Cell* **31**, 286–299 (2017).
41. Mohammad, H. P. et al. A DNA hypomethylation signature predicts antitumor activity of LSD1 inhibitors in SCLC. *Cancer Cell* **28**, 57–69 (2015).
42. Wu, B. et al. Epigenetic drug library screening identified an LSD1 inhibitor to target UTX-deficient cells for differentiation therapy. *Signal Transduct. Target. Ther.* **4**, 11 (2019).
43. Drost, J. et al. Organoid culture systems for prostate epithelial and cancer tissue. *Nat. Protoc.* **11**, 347–358 (2016).
44. Chen, C. et al. Cancer-associated IDH2 mutants drive an acute myeloid leukemia that is susceptible to Brd4 inhibition. *Genes Dev.* **27**, 1974–1985 (2013).
45. Buenrostro, J. D., Giresi, P. G., Zaba, L. C., Chang, H. Y. & Greenleaf, W. J. Transposition of native chromatin for fast and sensitive epigenomic profiling of open chromatin, DNA-binding proteins and nucleosome position. *Nat. Methods* **10**, 1213–1218 (2013).
46. Chen, M. et al. An epigenetic mechanism underlying chromosome 17p deletion-driven tumorigenesis. *Cancer Discov.* **11**, 194–207 (2021).
47. Jiang, L. et al. Genomic landscape survey identifies *SRSF1* as a key oncogene in small cell lung cancer. *PLoS Genet.* **12**, e1005895 (2016).
48. Simpson, K. L. et al. A biobank of small cell lung cancer CDX models elucidates inter- and intratumoral phenotypic heterogeneity. *Nat. Cancer* **1**, 437–451 (2020).

Acknowledgements

We thank Ruizhan Tong and the members of the C.C.–L.Y. laboratory for their technical support and suggestions and the Core Facilities of West China Hospital. This work was supported by the National Key R&D Program of China (2017YFA0505600, C.C.), the National Natural Science Foundation of China (81522003, 82170171, 81770157 and 81570150, C.C.; 81570150, F.N.; 8210102196, J.C.), the Sichuan Science and Technology Program (2020YFQ0059, 2020ZYD002, 2018ZJ0077 and 2017TJPT0005, C.C.) and the 1.3.5. Project for Disciplines of Excellence, West China Hospital, Sichuan University (C.C.).

Author contributions

F.N., X.P., J.C. and X.C. designed and performed experiments, analyzed data and wrote the manuscript. M.W., P.C., L.Y., L.Zhang, A.Z., L.Zhao, S.D., M.Zhang, Yiyun Wang, B.W., J.Zheng, Yuying Wang, J.Xu, J.W., B.W., M.C., H.L., J.Xue, M.H., Y.G., J.Zhu, L.Zhou, Y.Zhang, M.Y., P.T., M.F. and Z.L. performed experiments and analyzed data. Z.X., Y.Zhao, H.Y., C.Z., Yuan Wang, J.H., S.Y., D.X., L.C., Q.Z., M.Zeng, S.W.L., Y.Lu, Y.Liu and Y.Wei provided resources and designed experiments. C.C. conceived the project, designed experiments, analyzed data and wrote the manuscript.

Competing interests

The authors declare no competing interests.

Additional information

Extended data is available for this paper at <https://doi.org/10.1038/s43018-022-00361-6>.

Supplementary information The online version contains supplementary material available at <https://doi.org/10.1038/s43018-022-00361-6>.

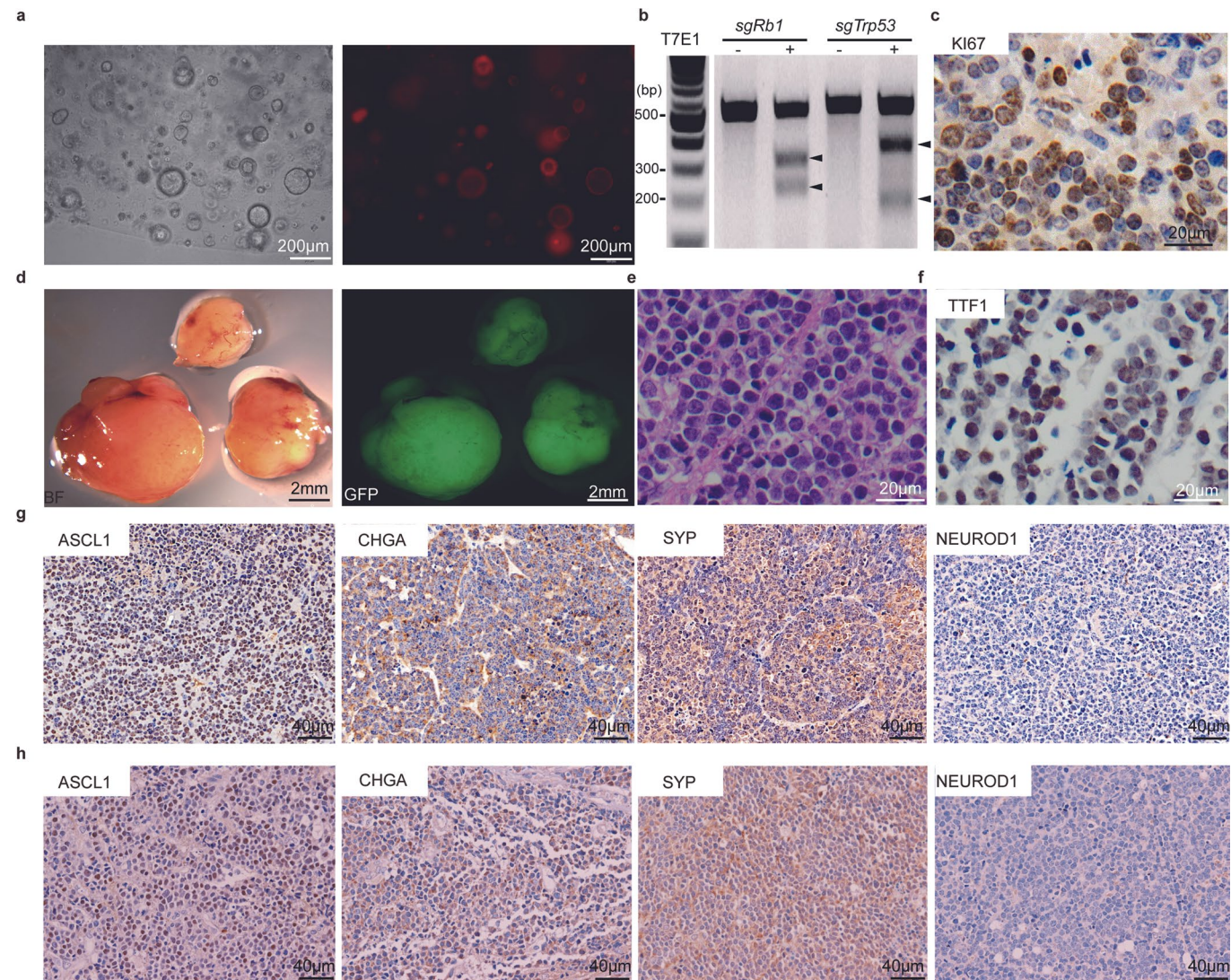
Correspondence and requests for materials should be addressed to Chong Chen.

Peer review information *Nature Cancer* thanks the anonymous reviewers for their contribution to the peer review of this work.

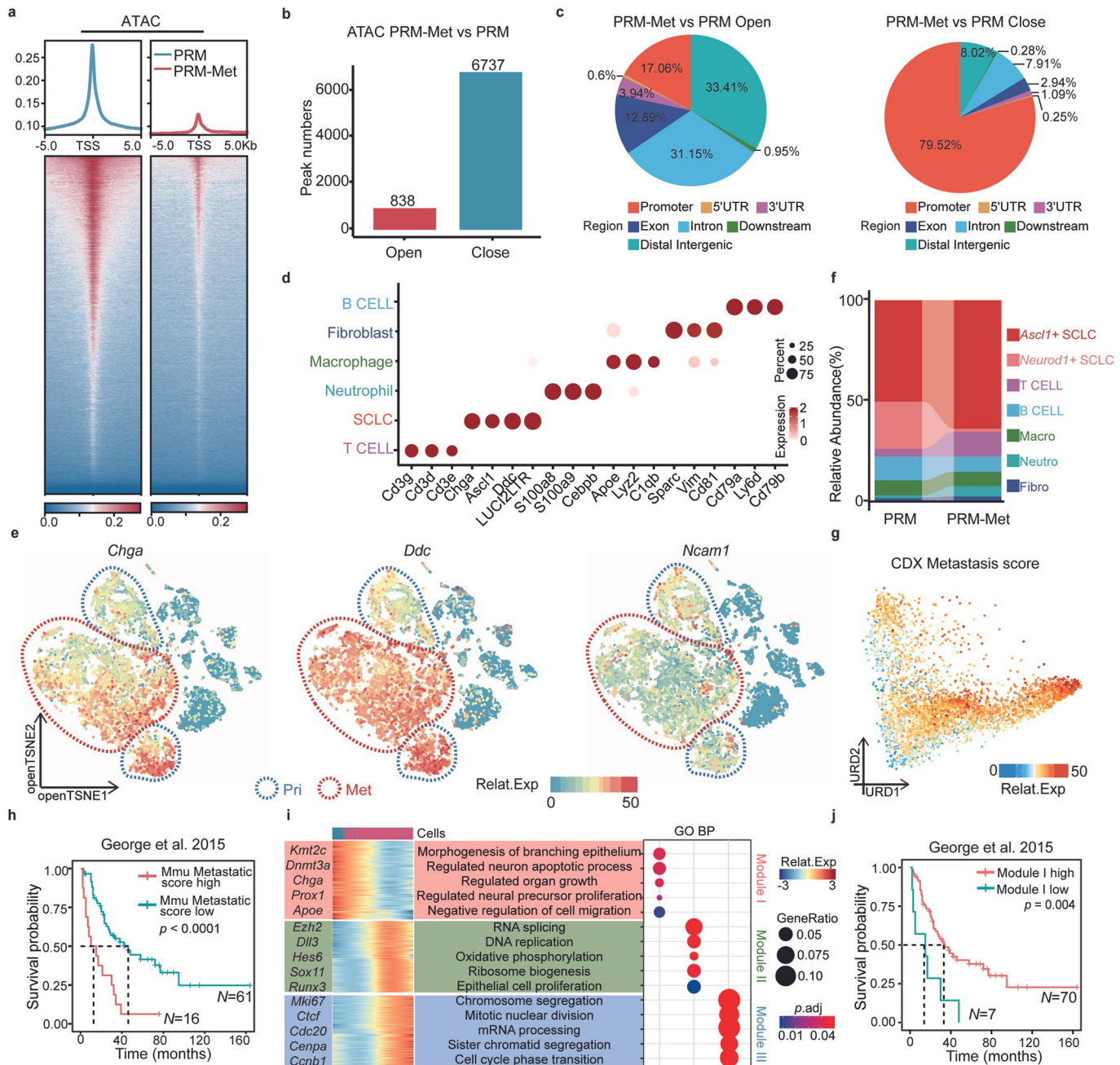
Reprints and permissions information is available at www.nature.com/reprints.

Publisher's note Springer Nature remains neutral with regard to jurisdictional claims in published maps and institutional affiliations.

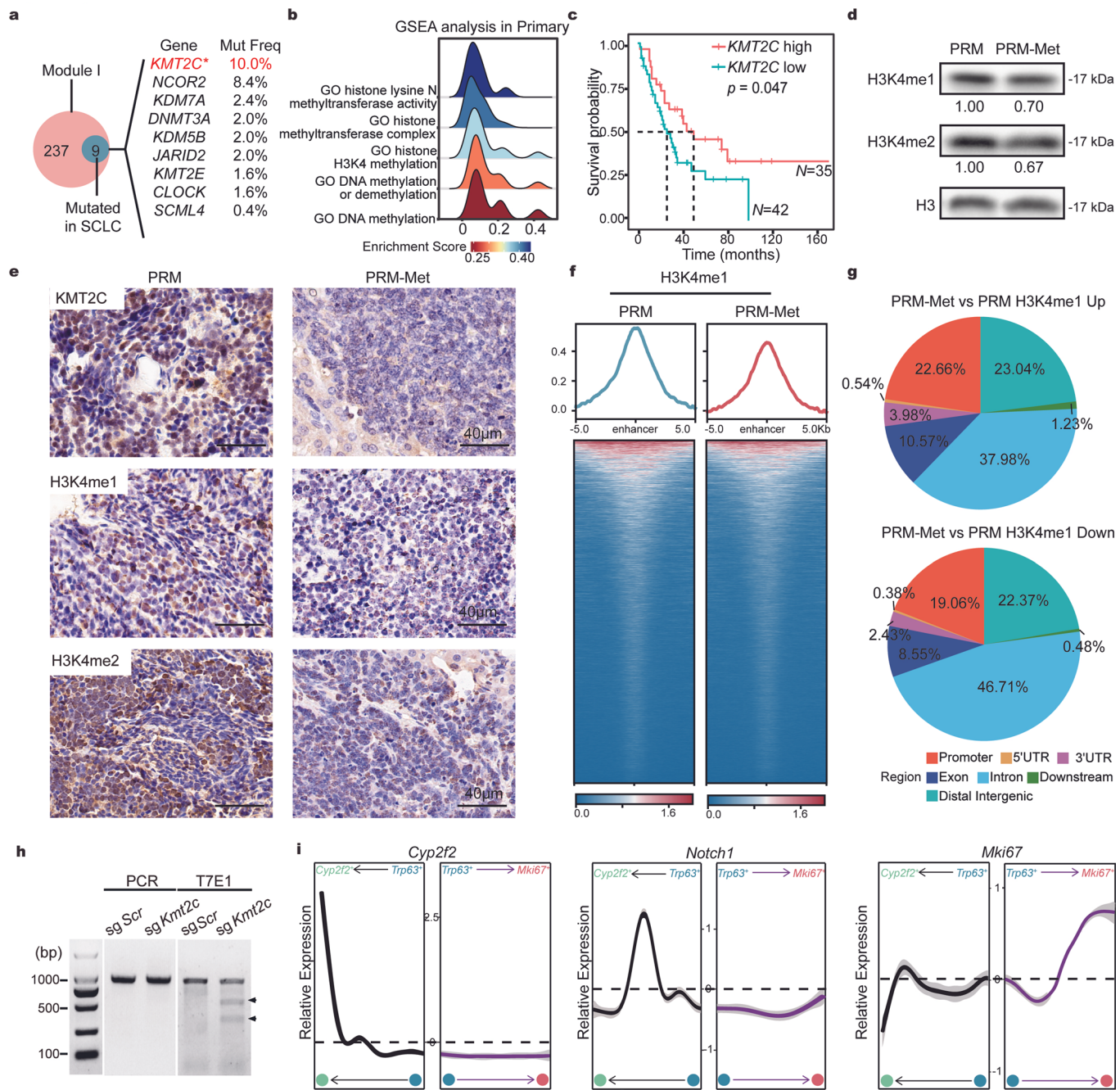
© The Author(s), under exclusive licence to Springer Nature America, Inc. 2022



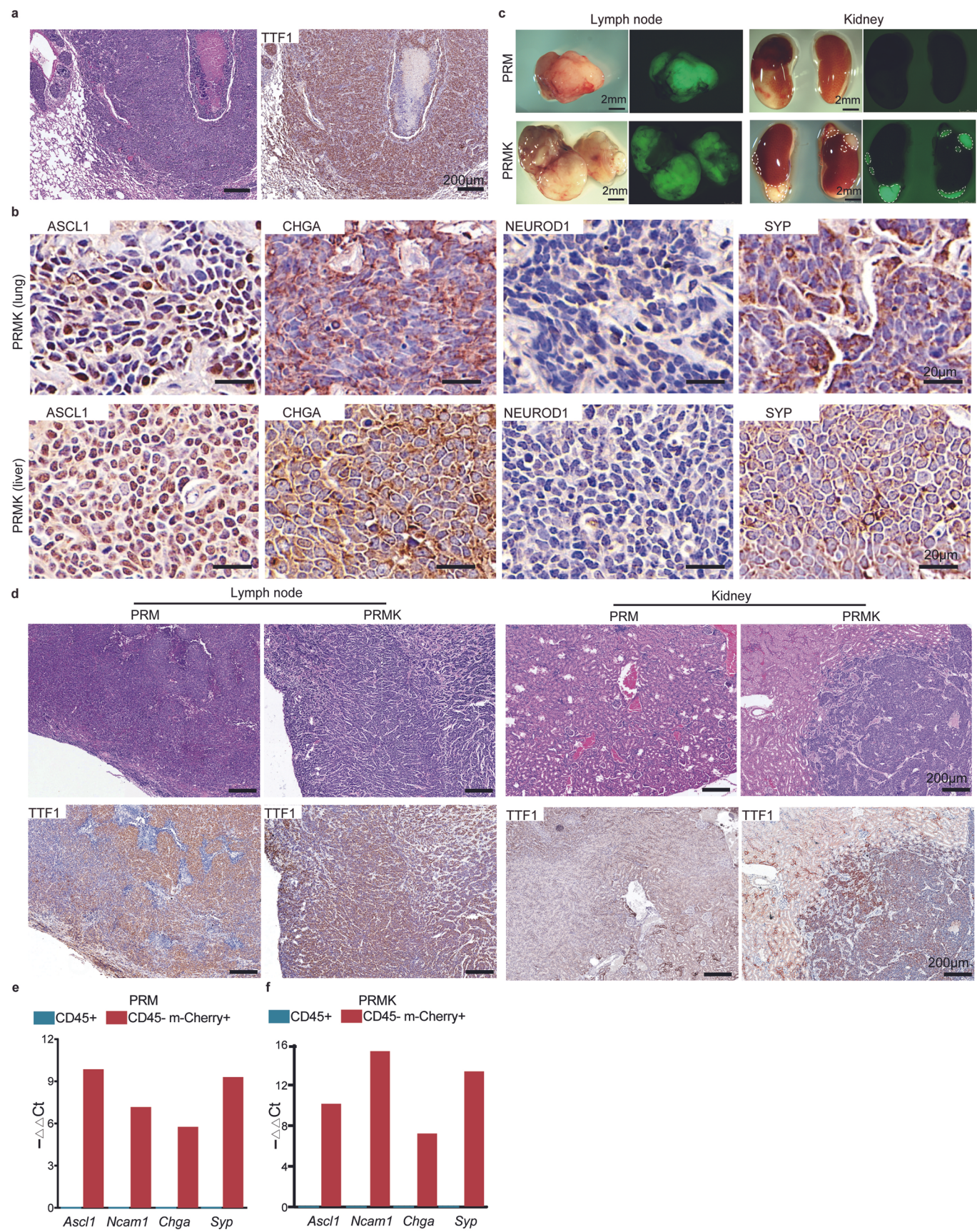
Extended Data Fig. 1 | Generating primary and orthotopic SCLC with metastases with genome edited lung organoids in mice. (a) Representative bright-field and fluorescent images of lung organoids transduced with V2TC-sgRNAs and Myc. Three independent repeats. Scale bar, 200 μ m. (b) T7 endonuclease 1 (T7E1) assays on *Rb1* or *Trp53* using infected lung organoid. Cleaved bands were pointed by arrowheads. Three independent repeats. (c) Representative IHC staining of KI67 of lung sections of the PRM mice ($n=4$ mice). Scale bar, 20 μ m. (d) Representative bright-field and fluorescent images showing metastatic lesions in the lymph nodes of the PRM mice ($n=4$ mice). Scale bar, 2 mm. (e) Representative H&E staining of the lymph nodes ($n=4$ mice). Scale bar, 20 μ m. (f) Representative TTF1 staining of the lymph nodes ($n=4$ mice). Scale bar, 20 μ m. (g) Representative pictures showing staining of ASCL1, CHGA, SYP and NEUROD1 of liver sections of the PRM mice ($n=4$ mice). Scale bar, 40 μ m. (h) Representative pictures showing staining of ASCL1, CHGA, SYP and NEUROD1 of the PRM mice's lymph node ($n=4$ mice). Scale bar, 40 μ m.



Extended Data Fig. 2 | Single-cell transcriptome analyses of primary and metastatic SCLC cells. (a) The ATAC-Seq plot showing signals at the TSS of the PRM and PRM-Met SCLC cells. (b) The bar graph showing the numbers of differential chromatin accessible peaks in the PRM and PRM-Met tumor cells. (c) Genome-wide distribution of chromatin open peaks (left) and close peaks (right) in PRM-Met compared to PRM, measured by ATAC-seq analyses. (d) The dot plot showing the marker genes of each cell type. (e) The openTSNE maps showing the expression distributions of *Chga*, *Ddc* and *Ncam1*. (f) The Alluvial plot showing the composition variation of cell populations in PRM and PRM-Met. (g) The URD map showing the CDX metastasis score projected on the metastasis trajectory. (h) The Kaplan-Meier survival curves of SCLC patients with low and high mouse metastatic scores. *p*-value was calculated by log-rank test ($n=61$, low; $n=16$, high). (i) The dynamically expressed genes and enriched gene signatures on the metastasis trajectory. (j) The Kaplan-Meier survival curves of SCLC patients with low and high Module I gene signatures. *p*-value was calculated by log-rank test ($n=7$, low; $n=70$, high).

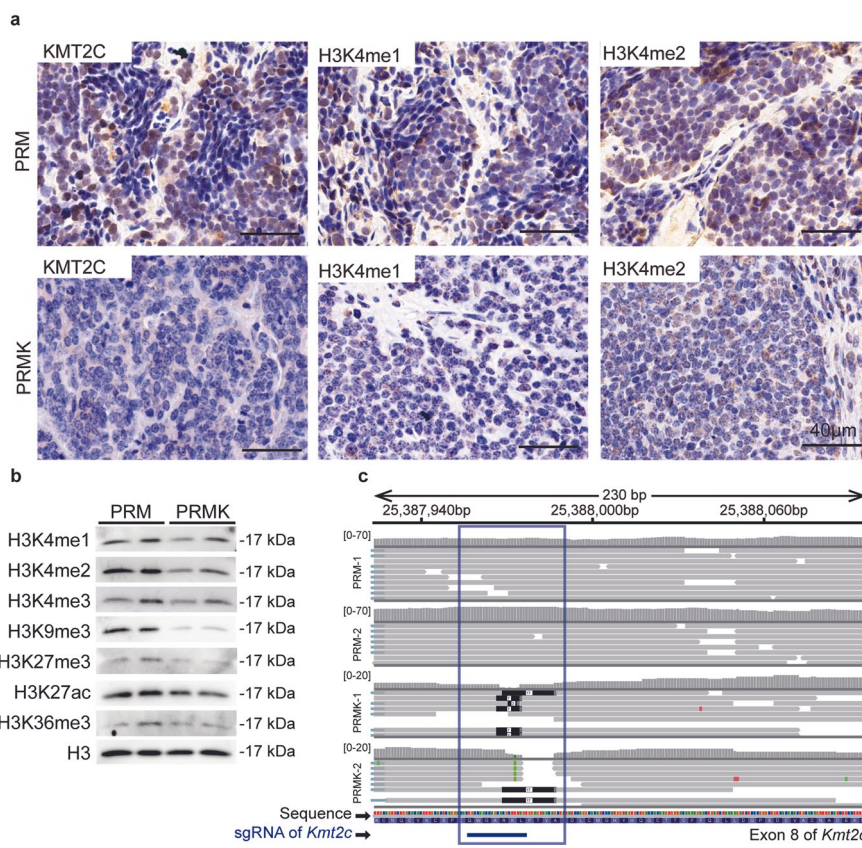


Extended Data Fig. 3 | KMT2C deficiency in SCLC metastases and its function in lung organoids. (a) The Venn plot showing the mutation frequency of epigenetic regulatory genes in Module I. (b) The Ridge plot showing gene ontology enrichment in the Ascl1 + primary SCLC cells, analyzed by GSEA. (c) The Kaplan-Meier survival curves of SCLC patients with low and high expressions of KMT2C. Calculated by log-rank test. ($n=42$, low; $n=35$, high) (d) Representative western blotting pictures of H3K4me1 and H3K4me2 in the PRM and PRM-Met SCLC cells. Three independent repeats. (e) Representative staining of KMT2C, H3K4me1 and H3K4me2 of the PRM primary ($n=3$) (left) and PRM-Met ($n=3$) liver sections (right). Scale bar, 40 μ m. (f) The levels of H3K4me1 bound at the enhancers in the PRM and PRM-Met tumor cells, measured by the CUT&Tag analyses. (g) Genome-wide distribution of the H3K4me1 up-regulated genes (top) and down-regulated genes (bottom) in PRM-Met compared to PRM, measured by CUT&Tag analyses. (h) T7 endonuclease 1 (T7E1) assays showing the mutations of *Kmt2c* in the premalignant PRM organoids. Three independent repeats. Cleaved bands were pointed by arrowheads. (i) Dynamics of relative expression levels of *Cyp2f2*, *Notch1* and *Mki67* on the normal development (black line) and malignant transformation (purple line) trajectories.

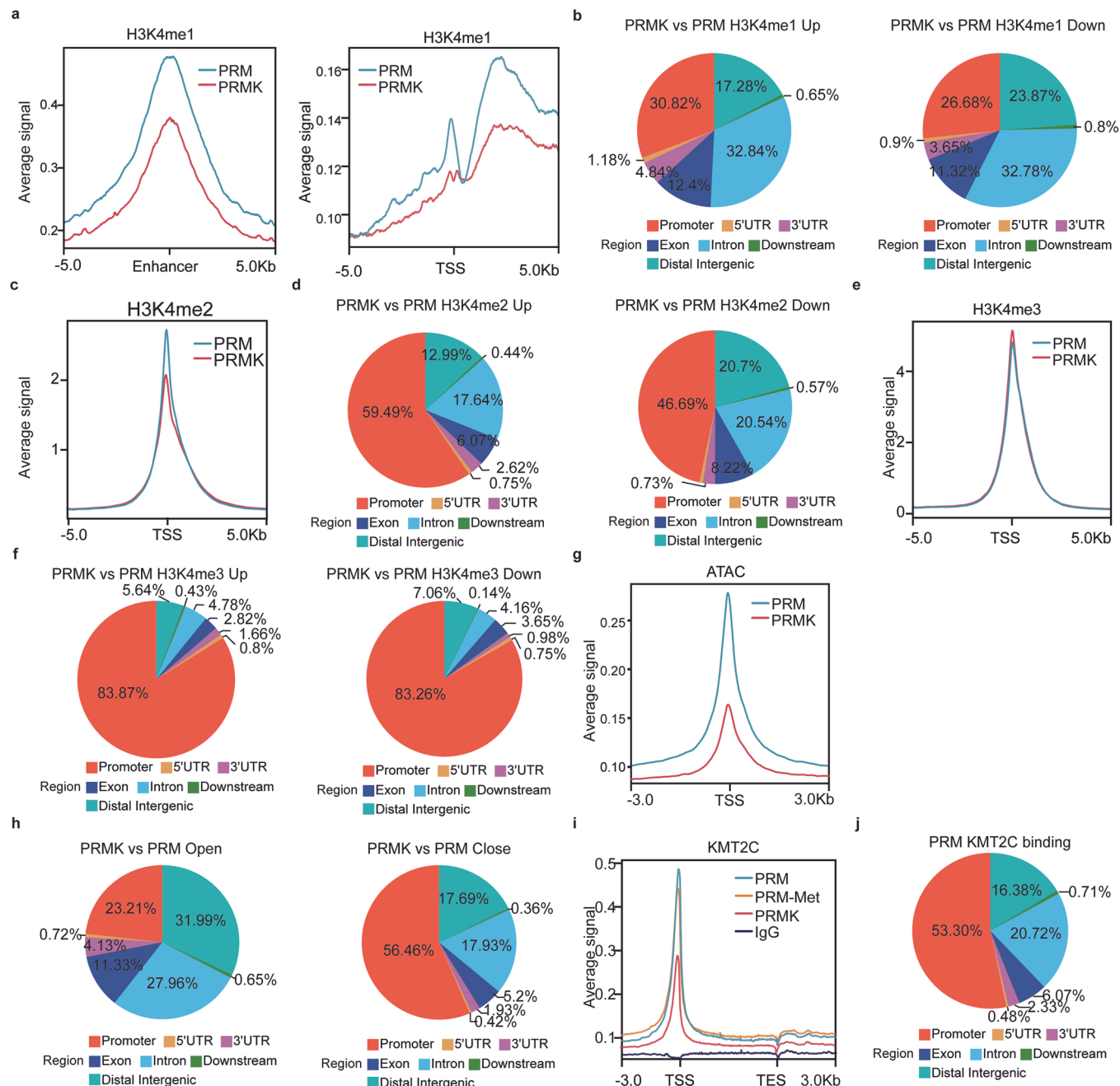


Extended Data Fig. 4 | See next page for caption.

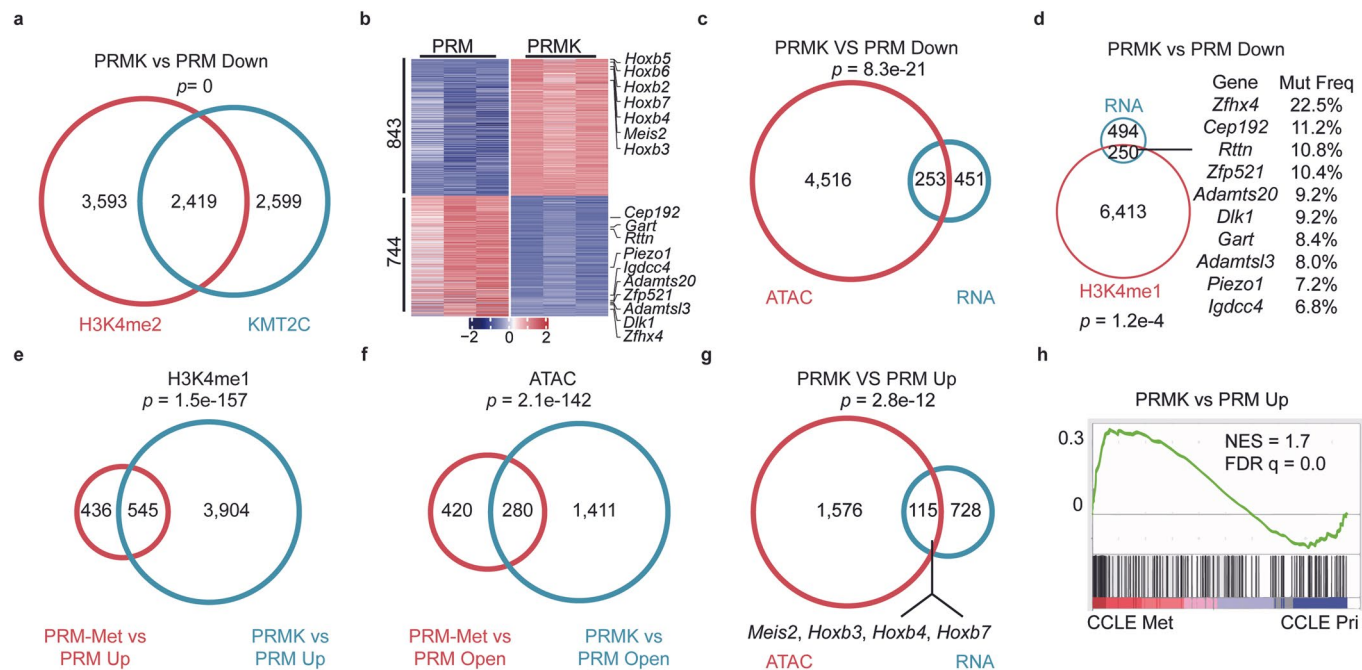
Extended Data Fig. 4 | Pathological analysis of the metastases in the PRM and PRMK mice. **(a)** Representative H&E (left) and TTF1 staining (right) of the lung sections of the PRMK mice ($n=4$ mice). Scale bar, 200 μm . **(b)** Representative staining of ASCL1, CHGA, NEUROD1 and SYP of the lung (top) and liver (bottom) sections of the PRMK mice ($n=4$ mice). Scale bar, 20 μm . **(c)** Representative images of the lymph nodes (left) and kidney (right) of the PRM ($n=4$) (top) and PRMK ($n=4$) (bottom) mice. Scale bar, 2 mm. **(d)** Representative H&E (top) and TTF1 staining (bottom) of the PRM ($n=4$) and PRMK ($n=4$) mice's lymph nodes (left) and kidney (right) sections. Scale bar, 200 μm . **(e)** The $-\Delta\Delta\text{CT}$ value of SCLC marker genes *Ascl1*, *Ncam1*, *Chga* and *Syp* in the CTC of PRM mice, measured by RT-qPCR ($n=3$ technical replicates). **(f)** The $-\Delta\Delta\text{CT}$ value of SCLC marker genes *Ascl1*, *Ncam1*, *Chga* and *Syp* in the CTC of PRMK mice, measured by RT-qPCR ($n=3$ technical replicates).



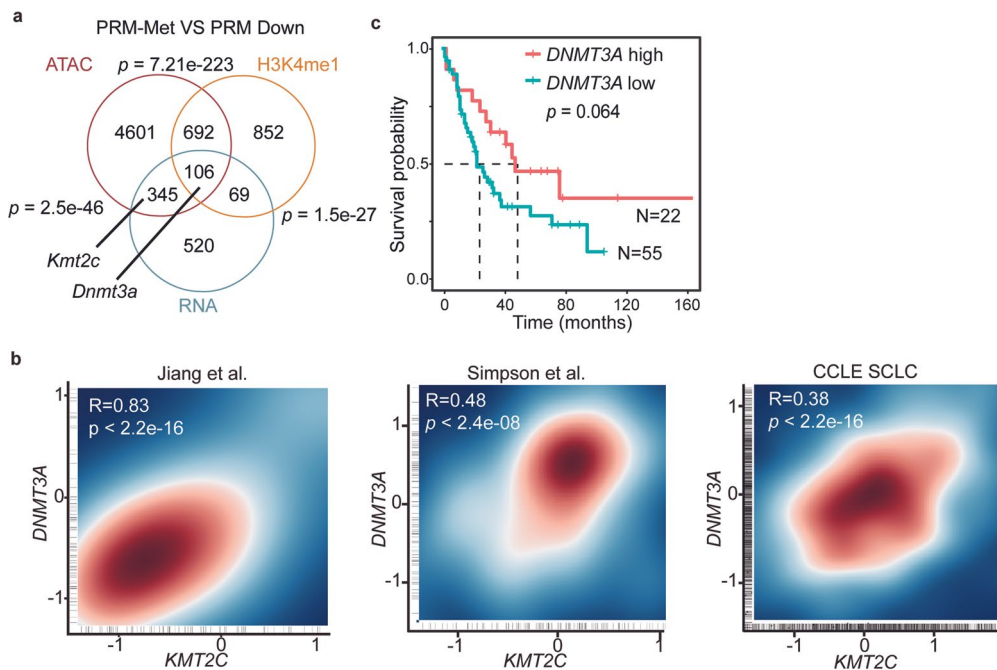
Extended Data Fig. 5 | The histone methylation in the PRM and PRMK SCLC. **(a)** Representative staining of KMT2C, H3K4me1 and H3K4me2 of the lung sections of PRM ($n=3$ mice) (top) and PRMK ($n=3$ mice) (bottom). Scale bar, 40 μ m. **(b)** Representative western blotting pictures showing the H3k4me1, H3k4me2, H3K4me3, H3K9me3, H3K27me3, H3K27ac and H3K36me3 levels in the PRM and PRMK SCLC cells. Three independent repeats. **(c)** The IGV plots showing the mutations and expression levels of *Kmt2c* in the PRM and PRMK SCLC.



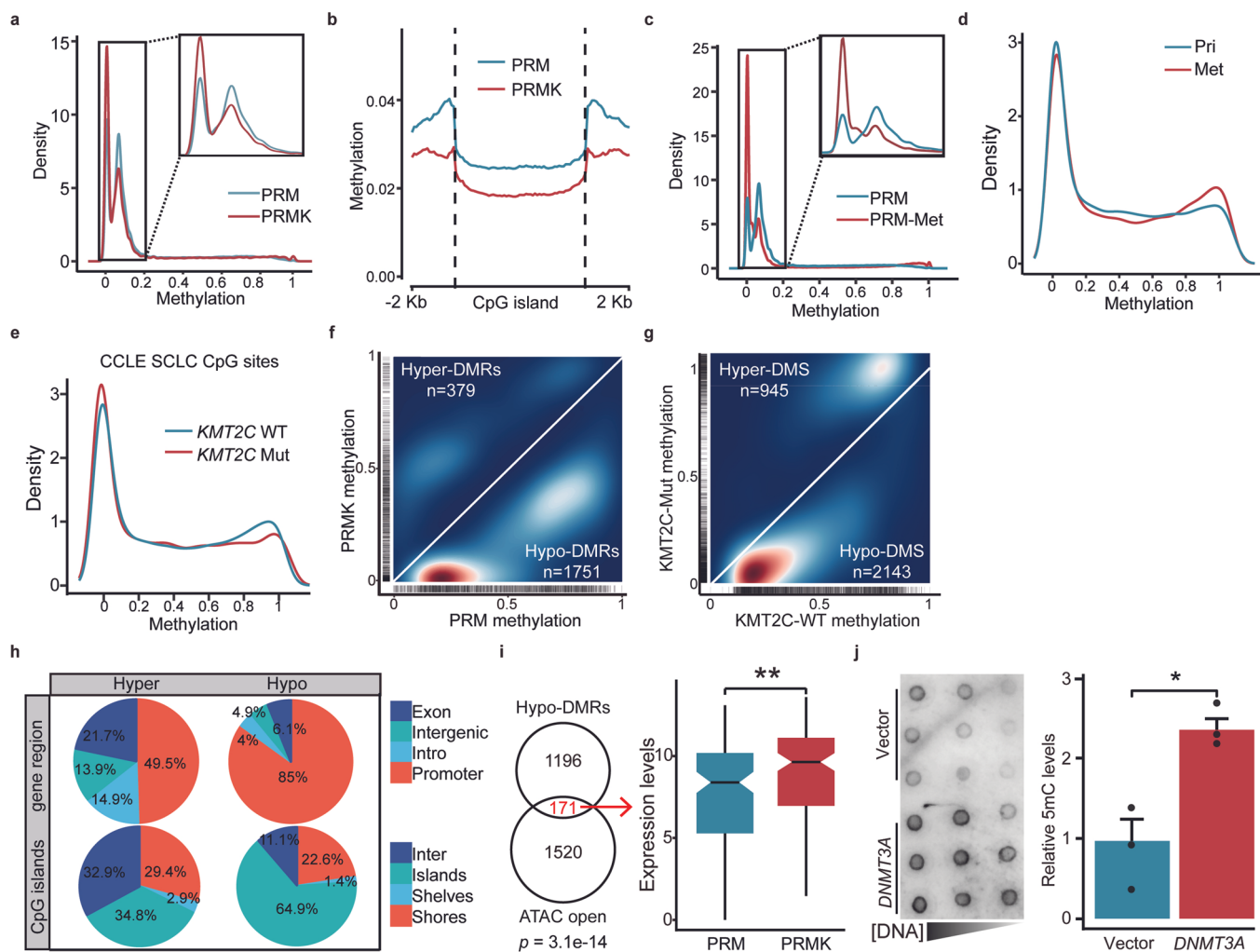
Extended Data Fig. 6 | The epigenetic reprogramming in SCLC with Kmt2c loss. **(a)** The levels of H3K4me1 bound at the enhancer (left) and TSS (right) in the PRM and PRMK SCLC cells, measured by CUT&Tag analyses. **(b)** Genome-wide distribution of the H3K4me1 up-regulated genes (left) and down-regulated genes (right) in PRMK compared to PRM, measured by CUT&Tag analyses. **(c)** The levels of H3K4me2 bound at the TSS in the PRM and PRMK SCLC cells, measured by CUT&Tag analyses. **(d)** Genome-wide distribution of the H3K4me2 up-regulated genes (left) and down-regulated genes (right) in PRMK compared to PRM, measured by CUT&Tag analyses. **(e)** The levels of H3K4me3 bound at the TSS in the PRM and PRMK SCLC cells, measured by CUT&Tag analyses. **(f)** Genome-wide distribution of the H3K4me3 up-regulated genes (left) and down-regulated genes (right) in PRMK compared to PRM, measured by CUT&Tag analyses. **(g)** The levels of ATAC bound at the TSS in the PRM and PRMK SCLC cells, measured by CUT&Tag analyses. **(h)** Genome-wide distribution of the ATAC open genes (top) and close genes (bottom) in PRMK compared to PRM. **(i)** The levels of KMT2C bound at the peaks of gene body in the PRM, PRM-Met and PRMK tumor cells, measured by the CUT & Tag analyses. **(j)** Genome-wide distribution of the KMT2C binding peaks in PRM, measured by CUT&Tag analyses.



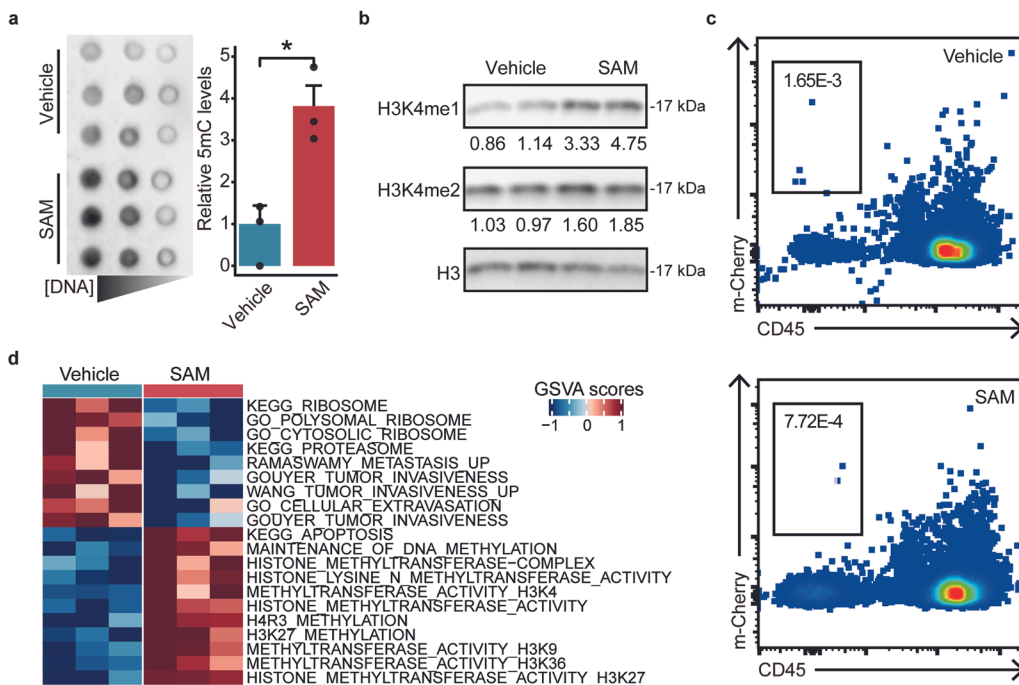
Extended Data Fig. 7 | The effect of epigenetic reprogramming on gene expressions in SCLC with *Kmt2c* loss. (a) The Venn diagram showing overlapping of the H3K4me2 down-regulated genes and the KMT2C down-regulated genes in PRMK compared to the PRM SCLC cells. p -value was calculated by a hypergeometric test. (b) Heatmap showing the differential expressed genes in the PRM and PRMK organoids. (c) The Venn diagram showing overlapping of the chromatin close genes and those downregulated in the PRMK cells compared to the PRM cells. p -value was calculated by a hypergeometric test. (d) The Venn diagram showing overlapping of the down-regulated genes and those with reduced H3K4me1 in the PRMK compared to the PRM cells. p -value was calculated by a hypergeometric test. (e) The Venn diagram showing overlapping of the H3K4me1 up-regulated genes in the PRM metastasis cells compared to the PRM primary cells and the H3K4me1 up-regulated genes in the PRMK cells compared to the PRM primary. p -value was calculated by a hypergeometric test. (f) The Venn diagram showing overlapping of the chromatin open genes in the PRM metastasis cells compared to the PRM primary cells and the chromatin open genes in the PRMK cells compared to the PRM primary. p -value was calculated by a hypergeometric test. (g) The Venn diagram showing overlapping of the chromatin open genes and those upregulated in the PRMK cells compared to the PRM cells. p -value was calculated by a hypergeometric test. (h) GSEA showing positive enrichment of the PRMK up-regulated gene set in the metastasis SCLC, compared to primary tumor cells in the CCLE cohort.



Extended Data Fig. 8 | Identifying DNMT3A as a downstream target of KMT2C in SCLC. **(a)** The Venn diagram showing overlapping of the down-regulated genes in RNA expression, chromatin accessibility, H3K4me1 in PRM-Met compared to PRM. p -value was calculated by a hypergeometric test. **(b)** The scatter plot showing the correlation between the relative expression levels of *KMT2C* and *DNMT3A* in multiple SCLC cohorts. **(c)** The Kaplan-Meier survival curves of SCLC patients with high or low expressions of *DNMT3A*. ($n=55$, low; $n=22$, high).



Extended Data Fig. 9 | KMT2C loss gave rise to DNA hypomethylation in SCLC. (a) The density plot showing all C sites' methylation levels in the genome of the PRM and PRMK SCLC cells. (b) The 5mC levels of the CpG regions in the PRM and PRMK cells. (c) The density plot showing all C sites' methylation levels in the genome of the PRM and PRM-Met SCLC cells. (d) The density plot showing the methylation levels of the CpG regions in the CCLE primary and metastasis SCLC cells. (e) The density plot showing the methylation levels of the CpG regions in the CCLE SCLC cells with or without KMT2C mutations. (f) The scatter plot showing the differentially methylated regions (DMRs) in the PRM and PRMK SCLC cells. (g) The scatter plot showing the differentially methylated sites (DMS) in the KMT2C-WT and KMT2C-Mut CCLE SCLC samples. (h) Pie charts showed the genomics region annotation (top) and CpGs subtypes (bottom) of hyper- and hypo- DMRs in PRMK compared to PRM. (i) The Venn diagram showed overlapping of the hypomethylated genes and open genes in PRMK compared to PRM (left); p-value was calculated by a hypergeometric test. The box plot displayed the normalized expression levels of 171 overlap genes of hypomethylated genes and open genes in PRM and PRMK (right), The box bounds the interquartile range divided by the median, with the whiskers extending to a maximum of 1.5 times the interquartile range beyond the box. p-value was calculated by Wilcoxon signed-rank test. (j) Dot blotting showed the expression of 5mC in PRMK organoids with vector or DNMT3A overexpression (left). The statistics of DNA 5mC levels in PRMK cells (right). (mean \pm SEM, n=3). Calculated by Student's t-test, two-sided. All p-value, *, p < 0.05.



Extended Data Fig. 10 | SAM treatment for KMT2C deficient SCLC. **(a)** The dot blotting (left) and the relative levels (right) of 5mC in the PRMK organoids treated with vehicle or SAM. (mean \pm SD, n=3). *, p < 0.05, Calculated by Student's t-test, two-sided. **(b)** The representative western blotting pictures showing the H3k4me1 and H3k4me2 levels in the PRMK organoids treated with vehicle or SAM. Three independent repeats. **(c)** The representative flow cytometry plots of CTCs in the peripheral blood of PRMK mice treated with vehicle or SAM. **(d)** Heatmap showing the differential pathways in SAM treated PRMK SCLC cells compared to those treated with vehicle, measured by RNA-seq analyses.

Reporting Summary

Nature Portfolio wishes to improve the reproducibility of the work that we publish. This form provides structure for consistency and transparency in reporting. For further information on Nature Portfolio policies, see our [Editorial Policies](#) and the [Editorial Policy Checklist](#).

Statistics

For all statistical analyses, confirm that the following items are present in the figure legend, table legend, main text, or Methods section.

n/a Confirmed

- The exact sample size (n) for each experimental group/condition, given as a discrete number and unit of measurement
- A statement on whether measurements were taken from distinct samples or whether the same sample was measured repeatedly
- The statistical test(s) used AND whether they are one- or two-sided
Only common tests should be described solely by name; describe more complex techniques in the Methods section.
- A description of all covariates tested
- A description of any assumptions or corrections, such as tests of normality and adjustment for multiple comparisons
- A full description of the statistical parameters including central tendency (e.g. means) or other basic estimates (e.g. regression coefficient) AND variation (e.g. standard deviation) or associated estimates of uncertainty (e.g. confidence intervals)
- For null hypothesis testing, the test statistic (e.g. F , t , r) with confidence intervals, effect sizes, degrees of freedom and P value noted
Give P values as exact values whenever suitable.
- For Bayesian analysis, information on the choice of priors and Markov chain Monte Carlo settings
- For hierarchical and complex designs, identification of the appropriate level for tests and full reporting of outcomes
- Estimates of effect sizes (e.g. Cohen's d , Pearson's r), indicating how they were calculated

Our web collection on [statistics for biologists](#) contains articles on many of the points above.

Software and code

Policy information about [availability of computer code](#)

Data collection

All software used for data collection is commercially available and stated in the Methods section. For RNA-seq, ATAC-seq, CUT&Tag, WGBS and scRNA-seq data collection, Illumina NovaSeq platform was used. For FACS data collection, Flow cytometry analysis was performed on Fortessa machines (BD Bioscience) and analyzed with Flowjo. Real-time quantitative PCR (RT-qPCR) was performed in QuantStudioTM 3 (Applied Biosystems). Micro-CT was performed using a small animal Quantum FX Micro-CT (PerkinElmer) and images were acquired and analyzed with PerkinElmer Quantum FX software. For bioluminescent imaging, mice were imaged on the IVIS Spectrum In Vivo Imaging System (PerkinElmer).

Data analysis

R(v3.6.1), IGV(v2.7.0), DESeq2(v1.26.0), STAR(v2.6.0a), pheatmap(v1.0.12), GSEA(v3.0), clusterProfiler(v3.14.3), BS-Seeker2(v2.1.8), GATK(v4.1.3), Bismark(v0.22.3), methylKit(v1.12.0), metilene(v0.2-7), ViewBS(v0.1.9), Bowtie2(v2.2.1), HMMRATAC(v1.2.5), NGmerge(v0.3), samtools(v1.8), SEACR(v1.3), ChIPseeker(v1.22.1), Deeptools(v3.5.1), diffReps(v1.55.6), cellranger(v2.1.1), Seurat(v3.2.0), Monocle2(v2.14.0), slingshot(v1.4.0). Details can be found in the methods section under "RNA-seq analyses", "Whole Genome Bisulfite Sequencing (WGBS) analyses", "ATAC-seq analyses", "Cleavage Under Targets and Tagmentation (CUT&TAG) analyses", "Single-cell RNA-seq analyses", "Omics data analyses of SCLC patients and cell lines". The analysis codes can be found in GitHub (<https://github.com/pangxueyu233/KMT2C-in-SCLC-Metastasis>).

For manuscripts utilizing custom algorithms or software that are central to the research but not yet described in published literature, software must be made available to editors and reviewers. We strongly encourage code deposition in a community repository (e.g. GitHub). See the Nature Portfolio [guidelines for submitting code & software](#) for further information.

Data

Policy information about [availability of data](#)

All manuscripts must include a [data availability statement](#). This statement should provide the following information, where applicable:

- Accession codes, unique identifiers, or web links for publicly available datasets
- A description of any restrictions on data availability
- For clinical datasets or third party data, please ensure that the statement adheres to our [policy](#)

The RNA-seq, ATAC-seq, CUT&TAG, WGBS and scRNA-seq data in this study are deposited in NCBI GEO: GSE161570. The processed files were submitted in Figshare(<https://figshare.com/articles/dataset/>)

A_Coherent_Histone_and_DNA_Hypomethylation_Reprogramming_Drives_Small_Cell_Lung_Cancer_Metastasis/13206338). The genomics data of SCLC were downloaded from cBioPortal (<https://www.cbioportal.org/>). The omics data of 39 SCLC cell lines were accessed from the CCLE database of depmap portal (<https://depmap.org/portal>), including the mutation, CpG methylation, RNA-seq and annotation information. The RNA-seq data and clinical data of 81 SCLC patients were downloaded from Julie et al., (doi:10.1038/nature14664). The RNA-seq data of 86 SCLC patients were downloaded from Liyan et al., (doi:10.1371/journal.pgen.1005895). The RNA-seq data of 120 SCLC CDX data were downloaded from Kathryn et al., (doi: 10.5281/zenodo.3574846). The single-cell RNA-seq data of SCLC patients were downloaded from C. Allison., (doi:10.1038/s43018-019-0020-z).

Field-specific reporting

Please select the one below that is the best fit for your research. If you are not sure, read the appropriate sections before making your selection.

Life sciences Behavioural & social sciences Ecological, evolutionary & environmental sciences

For a reference copy of the document with all sections, see nature.com/documents/nr-reporting-summary-flat.pdf

Life sciences study design

All studies must disclose on these points even when the disclosure is negative.

Sample size	For in vitro study we perform three independent experiments. For in vivo study sample sizes per group varied from 3 to 9 depending on number of animals with tumours available.
Data exclusions	No data were excluded from the study.
Replication	All experiments were reliably reproduced. For CUT&TAG-seq data, WGBS-seq data and ATAC-seq data, two independent replicates were used in case and control group. For RNA-seq data, at least three independent samples were used as replicates. For scRNA-seq the primary and metastases sample were performed the same steps for library construction and the same analysis pipelines for data analyzing. All analysis codes were available.
Randomization	For the in vivo treatment experiments, the starting tumor burden in the treatment and control groups was similar before treatment. For the in vitro treatment experiments, all samples were randomly assigned to vehicle or treatment group.
Blinding	Tumor measurements were performed blindly. The description of organoid shapes and the number of metastases were analyzed blindly. For other in vivo and in vitro experiments, the researchers were not blinded when performing the experiments.

Reporting for specific materials, systems and methods

We require information from authors about some types of materials, experimental systems and methods used in many studies. Here, indicate whether each material, system or method listed is relevant to your study. If you are not sure if a list item applies to your research, read the appropriate section before selecting a response.

Materials & experimental systems

n/a	Involved in the study
<input type="checkbox"/>	<input checked="" type="checkbox"/> Antibodies
<input type="checkbox"/>	<input checked="" type="checkbox"/> Eukaryotic cell lines
<input checked="" type="checkbox"/>	<input type="checkbox"/> Palaeontology and archaeology
<input type="checkbox"/>	<input checked="" type="checkbox"/> Animals and other organisms
<input type="checkbox"/>	<input checked="" type="checkbox"/> Human research participants
<input checked="" type="checkbox"/>	<input type="checkbox"/> Clinical data
<input checked="" type="checkbox"/>	<input type="checkbox"/> Dual use research of concern

Methods

n/a	Involved in the study
<input type="checkbox"/>	<input checked="" type="checkbox"/> ChIP-seq
<input type="checkbox"/>	<input checked="" type="checkbox"/> Flow cytometry
<input checked="" type="checkbox"/>	<input type="checkbox"/> MRI-based neuroimaging

Antibodies

Antibodies used	TTF1 Abcam 1:250 #ab76013 MUC1 Abcam 1:500 #ab45167 Aquaporin5 Abcam 1:500 #ab78486 EdU RIBOBIO #C10310-3 Ascl1 BD Pharmingen 1:100 #556604 Synaptophysin Abcam 1:500 #ab32127 Chromogranin A Abcam 1:400 #ab15160 NEUROD1 Abcam 1:200 #ab109224 Ki67 BD Pharmingen 1:200 #550609 P63 Abcam 1:100 #ab735 PB-CD45.2 BioLegend 1:200 #109820 H3K4me1 Abcam 1:400(IHC), 1:2000 (western blotting) #ab8895 H3K4me2 Abcam 1:400(IHC), 1:2000 (western blotting) #ab7766 H3K4me3 Abcam 1:50 (CUT&TAG), 1:1000 (western blotting) #ab8580 H3K4me3 ABclonal 1:50 (IHC) #A2357 H3K9me3 Abcam 1:2000 (western blotting) #ab8898 H3K27me3 Cellsignal 1:1000 (western blotting) #9733s H3K27ac Abcam 1:2000 (western blotting) #ab4729 H3K36me3 Cellsignal 1:1000 (western blotting) #4909s H3 HUABIO 1:3000 #EM30605 5mC antibody Active Motif 1:3000 #39649 KMT2C Abcam 1:400 #71200
Validation	All the antibodies are validated for the use of immunofluorescence, immunohistochemistry, WB and CUT&TAG analyses. Data are available on the manufacturer's website. The following primary antibodies have been validated by the manufacturer and/or in this paper: TTF: Immunohistochemistry on formalin-fixed paraffin embedded mouse tumor MUC: Whole-mount immunostaining of normal lung organoids Aquaporin: Whole-mount immunostaining of normal lung organoids EdU RIBOBIO: Whole-mount immunostaining of normal lung organoids Ascl: Immunohistochemistry on formalin-fixed paraffin embedded mouse tumor Synaptophysin: Immunohistochemistry on formalin-fixed paraffin embedded mouse tumor Chromogranin : Immunohistochemistry on formalin-fixed paraffin embedded mouse tumor NEUROD1: Immunohistochemistry on formalin-fixed paraffin embedded mouse tumor Ki6: Immunohistochemistry on formalin-fixed paraffin embedded mouse tumor P63: Immunohistochemistry on formalin-fixed paraffin embedded mouse tumor PB-CD45.2: Flow cytometric analysis of CD45.2 expression on mouse peripheral blood cell H3K4me1: IHC, Western blotting and CUT&TAG assay of SCLC tumor H3K4me2: IHC, Western blotting and CUT&TAG assay of SCLC tumor H3K4me3(Abcam): Western blotting and CUT&TAG assay of SCLC tumor H3K4me3(ABclonal):IHC. The informations about H3K4me3 antibody (ABclonal, A2357) are as follow : Description: Rabbit polyclonal to Histone H3 (tri methyl K4) ; Application: WB, IHC, IF, IP, ChIP, DB ; Reactivity: Human, Mouse, Rat. H3K9me3: Western blotting assay of SCLC tumor H3K27me3: Western blotting assay of SCLC tumor H3K27ac: Western blotting assay of SCLC tumor H3K36me3: Western blotting assay of SCLC tumor H: Western blotting assay of SCLC tumor 5mC antibody: DNA 5mC dot blotting assay of SCLC tumor KMT2C antibod: Immunohistochemistry on formalin-fixed paraffin embedded mouse tumor

Eukaryotic cell lines

Policy information about [cell lines](#)

Cell line source(s)	HEK-293T was purchased from ATCC
Authentication	No authentication was performed
Mycoplasma contamination	Cell line tested negative for mycoplasma
Commonly misidentified lines (See ICLAC register)	No commonly misidentified cell lines were used in the study

Animals and other organisms

Policy information about [studies involving animals](#); [ARRIVE guidelines](#) recommended for reporting animal research

Laboratory animals	Mice were kept in the SPF animal facility in Sichuan University with autoclaved food, bedding, and water. Animal housing room temperature: 23°C+/- degrees; humidity: 30-70%; light:6am-6pm. All the mouse experiments were performed in compliance with the Guide for the Care and Use of Laboratory Animals of Sichuan University, and approved by the Animal Care and Use Committee of
--------------------	---

Sichuan University. C57BL/6 (Jackson Lab, Cat# 000664) and CAG-Cas9-EGFP mice (Jackson Lab, Cat# 026179) (male, 8–10 weeks old and ~20 g weight) were used.

Wild animals

The study did not involve wild animals.

Field-collected samples

The study did not involve field-collected samples.

Ethics oversight

All the mouse experiments were performed in compliance with the Guide for the Care and Use of Laboratory Animals of Sichuan University, and approved by the Animal Care and Use Committee of Sichuan University.

Note that full information on the approval of the study protocol must also be provided in the manuscript.

Human research participants

Policy information about [studies involving human research participants](#)

Population characteristics

The extensive stage SCLC patients with hydrothorax were selected, regardless of age and gender. All patients had a confirmed pathologic diagnosis of SCLC. The information of the patients(HX20200923: Female, 49y, ES-SCLC, Upfront treatment: EP, Irinotecan, Radiotherapy; HX20201103: Male, 75y, ES-SCLC, Upfront treatment: EP, Radiotherapy)

Recruitment

Patients were recruited from the Department of Thoracic Oncology at West China Hospital, Sichuan University. Written agreements were provided by patients for hydrothorax extraction for research purpose. Extensive stage SCLC patients were encouraged to be recruited, regardless of age, gender and prior treatment.

Ethics oversight

This study complied with all relevant ethical regulations and was approved by the Ethics Committee on Biomedical Research, West China Hospital of Sichuan University. Written informed consents were provided by all participants.

Note that full information on the approval of the study protocol must also be provided in the manuscript.

ChIP-seq

Data deposition

Confirm that both raw and final processed data have been deposited in a public database such as [GEO](#).

Confirm that you have deposited or provided access to graph files (e.g. BED files) for the called peaks.

Data access links

May remain private before publication.

The CUT-tag data is available in GEO: GSE161570

Files in database submission

20 files

Genome browser session (e.g. [UCSC](#))

We will provide the link upon request and will be added to the manuscript prior to acceptance

Methodology

Replicates

two replicates

Sequencing depth

We sequenced for ~6G per sample of Illumina NovaSeq 6000 with 150-bp paired-end reads

Antibodies

H3k4me1 1:50 (#ab8895 Abcam), H3k4me2 1:50 (#ab7766, Abcam), H3k4me3 1:50 (#ab8580, Abcam), KMT2C 1:50 (#71200, Abcam)

Peak calling parameters

Reads were mapped to mm10 by Bowtie 2 (v2.3.4.2) with options: --local --very-sensitive --no-mixed --nodiscordant --phred33 -l 10-X 700. SEACR (v1.3) was used for peak calling. Differential histone modifications analysis was performed by diffReps and R package ChIPseeker was used to annotate the peaks regions.

Data quality

For KMT2C, a average number of 87,867 peaks in each sample were identified.

For H3K4me1, a average number of 33,349 peaks in each sample were identified.

For H3K4me2, a average number of 24,827 peaks in each sample were identified.

For H3K4me3, a average number of 17,354 peaks in each sample were identified.

Software

Bowtie2(v2.2.1), GATK(v4.1.3), SEACR(v1.3), diffReps(v1.55.6), DESeq2(v1.26.0), ChIPseeker(v1.22.1), DeepTools(v3.5.1), IGV(v2.7.0)

Flow Cytometry

Plots

Confirm that:

- The axis labels state the marker and fluorochrome used (e.g. CD4-FITC).
- The axis scales are clearly visible. Include numbers along axes only for bottom left plot of group (a 'group' is an analysis of identical markers).
- All plots are contour plots with outliers or pseudocolor plots.
- A numerical value for number of cells or percentage (with statistics) is provided.

Methodology

Sample preparation

Peripheral blood was obtained from retro-orbital puncture, and RBCs were lysed by ACK lysis buffer. Antibody (PB-CD45.2 (BioLegend, #109820)) staining was performed at 4°C for 30 min with PBS.

Instrument

BD LSRII Fortessa

Software

Flowjo software

Cell population abundance

Purity of populations from mouse peripheral blood was assessed by flow cytometry.

Gating strategy

FSC and SSC parameters were used to gate living cells as P1, followed with CD45-mCherry+ populations as SCLC CTC

- Tick this box to confirm that a figure exemplifying the gating strategy is provided in the Supplementary Information.